UNIVERSITÄT
LEIPZIG

Photocurrent-Based Study of Defects in Diamond

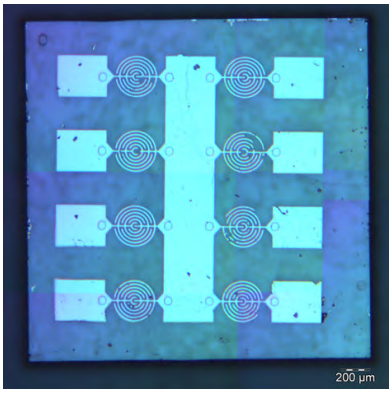

Bachelor Thesis

Submitted By
Tobias Erbacher
3755249

Supervisors
Prof. Dr. Jan Berend Meijer
Dr. Sébastien Pezzagna

Leipzig University
Faculty of Physics and Earth Sciences
Felix Bloch Institute for Solid State Physics
Applied Quantum Systems
Leipzig, February 9, 2023

— This page was intentionally left blank. —

Abstract

This Bachelor Thesis investigates the wavelength dependency of the photocurrent created in a diamond sample where various elements/molecules (B, C, CN, O, P, S) were implanted into separate spots on a 2×2 mm diamond sample to a depth of 30 to 60 nm. At the relevant locations, the surface was covered by a Palladium structure constructed using laser lithography. The sample can be seen on the cover page. In the next step, the photocurrent was measured by applying a bias voltage between the contacts of the Palladium structure and measuring the current while irradiating the sample with a laser beam, whose wavelength was varied, onto the implantation spots. Characteristic energies, at which the photocurrent begins for the respective implantations, were identified. Further, the dependence of the photocurrent on the bias voltage of some implantations as well as the relative order of maximum photocurrent was determined for the various implantations.

Table of Contents

List of Figures

List of Tables

1 Introduction

In 1921, Albert Einstein received the Nobel Prize for his explanation of the photoelectric effect,[1] where a photon can eject an electron from the material that it is incident upon. The flow of electrons, i. e. current, that is created by this mechanism is called photocurrent. However, it only occurs when the energy of each individual photon interacting with an electron is larger than the so-called work function, which is a material-dependent minimal amount of energy required to remove an electron from the material's surface. Albeit in the experiments that are part of this Bachelor Thesis, the photoelectrons are not entirely removed from the surface of the material but rather the photons excite them from the electronic valence band to the conduction band, where they then get picked up by the electrodes which are connected to an ampere meter.

This Bachelor Thesis aims to characterize various artificially implanted impurities in a diamond sample through the photocurrent that is created when illuminating the sample using an energy-tunable laser.

2 Theoretical Background

2.1 Carbon Atom and Diamond Lattice

The electronic configuration of a Carbon atom in its ground state[2] is $1s^2\ 2s^2\ 2p^2$, as depicted in figure 1 (a). In diamond (see fig. 1 (b)), all three 2p and the 2s orbitals hybridize into four sp^3 orbitals.[3] In bulk diamond, each of the four outermost orbitals

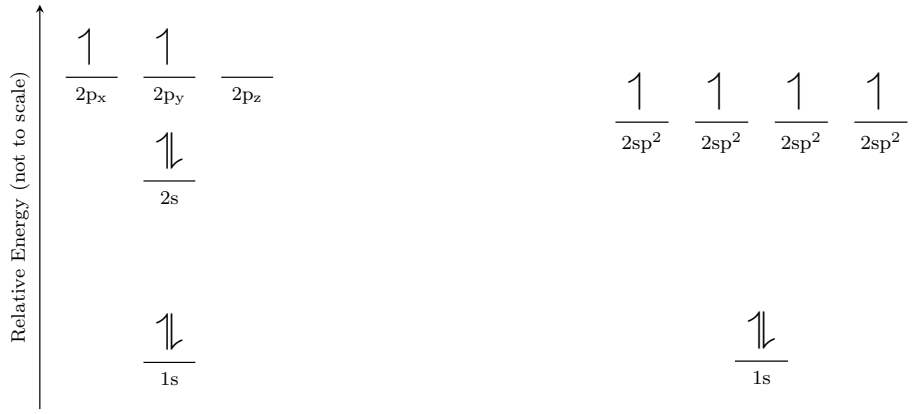

(a) Carbon ground state. (b) Diamond.

Figure 1: Electron configuration of Carbon and diamond.[4] Each arrow represents an electron and the arrows' orientation corresponds to the spin of the electrons.

(sp^3) is bound covalently to those of other Carbon atoms, with the atoms arranged as shown in figure 2 (a). This gives each individual Carbon atom's electron orbital a tetrahedral shape because it minimizes the required energy by placing the electrons as far away from each other, thereby reducing the repulsing Coulomb force. In particular, the angle between each of the electron orbital axes is 109.5°.[5] With a bond length of 1.54 Å,[6] the

diamond lattice is wider than the planar graphite bond length of 1.42 Å, but graphite's layer structure results in a relatively large inter-planar distance of 3.35 Å.[3] As a result, the diamond lattice is much more compact and thus its density of 3.51 g/cm^3 is higher than that of graphite with 2.27 g/cm^3.[5] Stacking the diamond unit cell components, depicted in figure 2 (a), diagonally, with empty cubes of the same size connected at their faces like a chess board, yields the unit cell drawn in figure 2 (b).

Nota bene: In graphite, the single-filled un-hybridized $2p_z$ orbital forms Pi bonds with that of its neighboring atoms in the planar hexagonal structure allowing these electrons to become delocalized which turns them into very good electrical and thermal conductors. Furthermore, there are many more energy transitions available to these delocalized electrons meaning they can absorb a wide variety of wavelengths of light and that makes graphite appear black, while in diamond all valence electrons are bound and therefore cannot move easily or have as many energetic transitions available. Hence, diamond appears transparent.

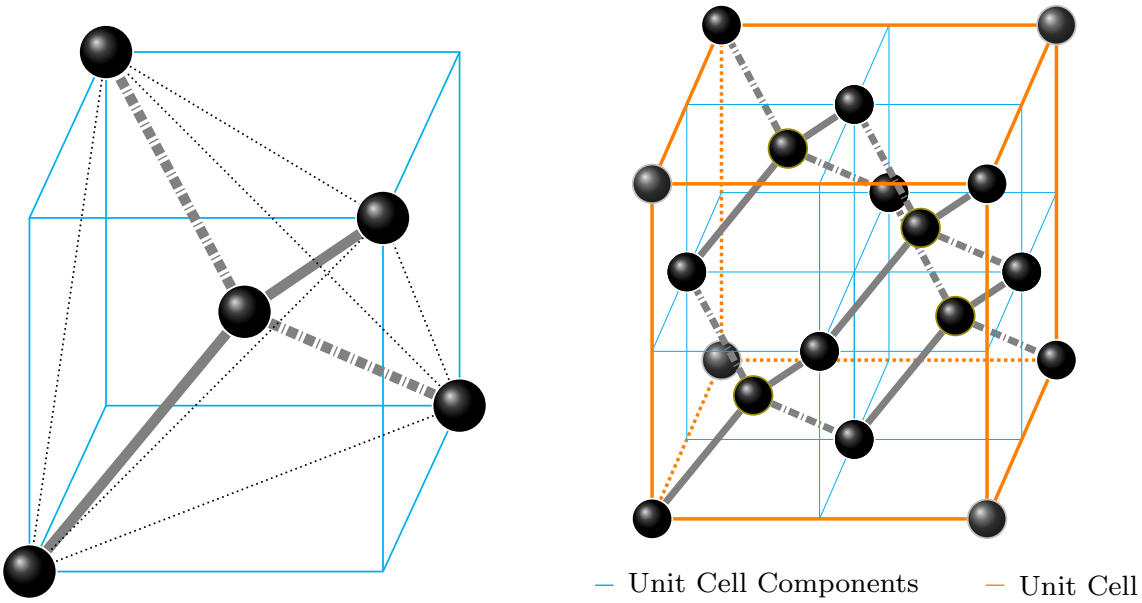

(a) Diamond unit cell component.

(b) Diamond unit cell.

Figure 2: Diamond cubic crystal structure with its constituent components. They are arranged such that every side faces an empty cube, while diagonally the components connect. The gray dashed lines point into the drawing plane, while the solid ones point outwards. Together, they indicate electronic bonding between the Carbon atoms, themselves shown as black spheres.[7]

2.2 Crystal Defects

Crystals rarely occur entirely in their pure form in nature, as there are usually some imperfections in the atomic structure. These can be intrinsic or extrinsic defects as well as vacancies, or a combination thereof. If a defect consists of an atom type that the crystal itself is made of, e. g. a Carbon defect in diamond, then this defect is called intrinsic. Consequently, if the defect is made of a different kind of atom, such as Nitrogen, then the defect is said to be extrinsic. These defects can appear as combinations, too, e. g. a Nitrogen-Vacancy defect. Further, these defects can have different charge states. Natural diamonds are classified mostly according to their Nitrogen concentration, as shown in table 1. Synthetic diamonds, however, can have a much wider variety of defects and need to be classified more precisely.

<table>
<tr><td colspan="3">Type I

N > 5 ppm,
typically 100 - 3000 ppm,
transparent down to 330 nm</td><td colspan="2">Type II

N < 5 ppm,
typically very low concentration,
transparent down to 220 nm</td></tr>
<tr><td colspan="2">Type I a

Aggregate
Nitrogen</td><td>Type I b

Single substitutional
Nitrogen</td><td>Type II a

Nitrogen is
major impurity</td><td>Type II b

Boron is
major impurity</td></tr>
<tr><td>Type I aA

Nitrogen
A-center</td><td>Type I aB

Nitrogen
B-center</td><td>Nitrogen
C-center</td><td colspan="2"></td></tr>
</table>

Table 1: Natural diamond type classification scheme.[8]

Having a band gap energy of approximately 5.4 - 5.5 eV,[9][10] which corresponds to a wavelength of $\lambda = \frac{hc}{E} \approx 225$ - 230 nm, pure diamond is transparent to visible light, as it ranges from 380 to 770 nm.[11] When introducing defects, such as those shown in table 1, the absorption edges can differ greatly from that of a pure, ideal diamond. In the experiments of this Bachelor Thesis, a type IIa diamond was used.

There are many more possible defects of the diamond structure and different combinations thereof can produce a great variety of colors in diamonds, also depending on the concentration of those impurities. Moreover, the absorption lines and bands in figures 3, 4 and 5 are only indicative, i. e. there may be similar absorption characteristics from different defects and it may therefore be difficult to ascribe a certain line or band to a particular defect. In these figures, e. g. Hydrogen-based defects are not shown as the plethora of absorption lines in the visible spectrum would require several graphs on their own. In the infra-red (IR) spectrum, the 3.22 µm line is most notable for Hydrogen defects.[17] Bearing in mind that all defects shown in figures 3, 4 and 5 are extrinsic and of substitutional nature, these can, however, also occur as interstitial defects that do not attach to a specific lattice site but rather remain stuck between other Carbon atoms of the diamond structure. During a heat treatment process called annealing, these interstitials are given enough energy so that they can find a new location and in that way repair the crystal to some extent.

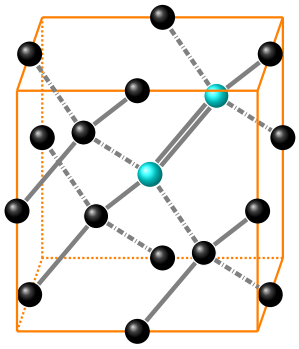

(a) A-center defect consisting of 2 substitutional Nitrogen atoms with a double bond.[12]

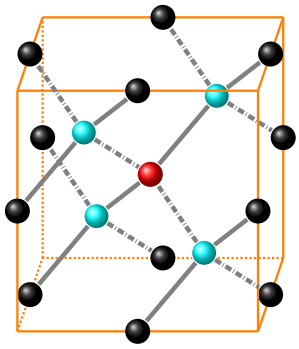

(b) B-center defect consisting of 4 substitutional Nitrogen atoms surrounding 1 Vacancy.[13]

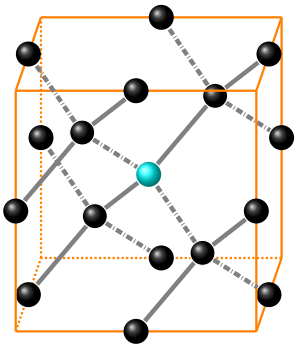

(c) C-center defect consisting of 1 substitutional Nitrogen atom.[13]

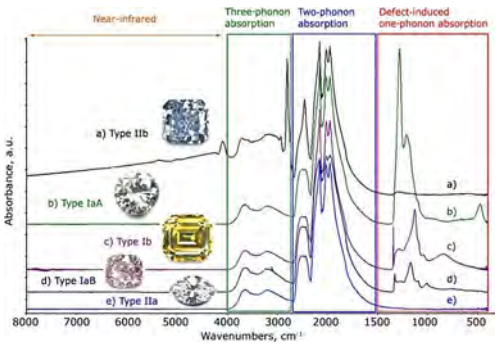

(d) IR absorbance spectrum. Intrinsic diamond absorbance between 4000 and 1500 cm^{-1} (2.50 to 6.67 µm), A-line at 1215 cm^{-1} (8.23 µm), B-line at 1175 cm^{-1} (8.51 µm) and C-line at 1135 cm^{-1} (8.81 µm).[14]

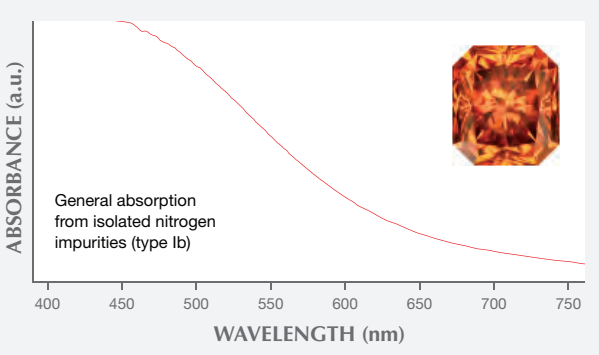

(e) C-center absorbance spectrum, which can introduce a yellow to brown color to the diamond.[15] A- and B- centers do not absorb in the visible range.[16]

Figure 3: A-, B- and C-center defects in diamond.

2.3 Implantation of Ions

Two of the three major challenges when aiming to implant ions are solved by using appropriate tools and parts; these are the creation of ions from uncharged atoms, and the handling of ions. The other challenge is the firing accuracy in the target.

Ion beams, in contrast to optical beams, cannot simply be reflected or focused using mirrors or lenses. Instead, accelerating and redirecting the constituent particles of the beam is achieved by subjecting them to electric and magnetic fields. Using finely tuned placements of combinations of these fields, the effects of mirrors and lenses can be emulated. The implantation setup will be explained in section 3.1.

Only the accuracy of ion deposition in the target presents a major issue. When an ion enters the target material, it will at some point collide with atoms from the target. Subsequently, it bounces off them and in almost all cases further collision ensue. This chaotic motion is very difficult to predict, as the direction of movement post-collision is extremely

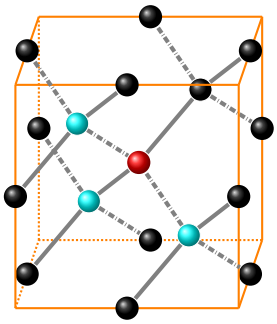

(a) N3 defect consisting of 3 Nitrogen atoms and 1 Vacancy.[12]

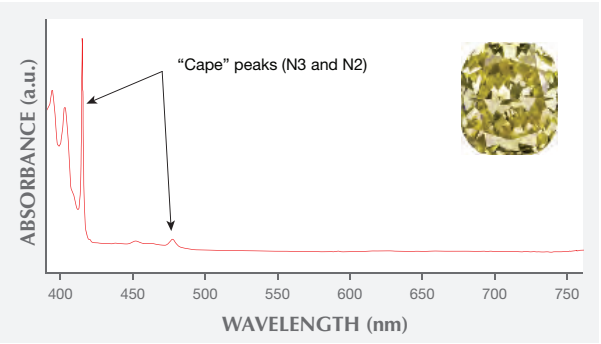

(b) N3 absorbance spectrum with the N3-line at 415.2 nm and N2-line at 477.2 nm.[17][15]

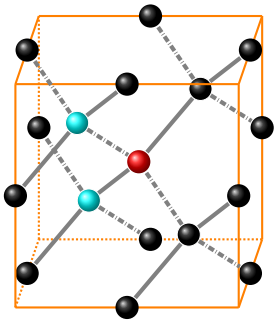

(c) H3 defect consisting of 2 Nitrogen atoms and 1 Vacancy.[18]

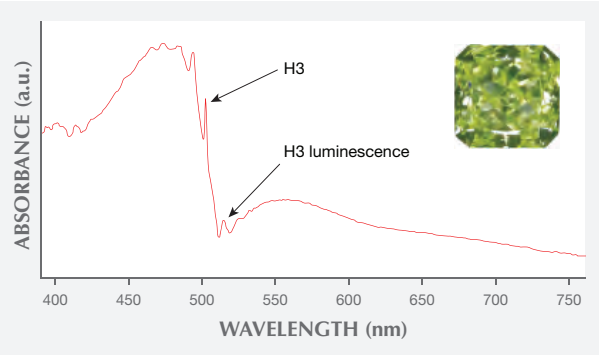

(d) H3 absorbance spectrum with the H3-line at 503.2 nm, broad absorption from 420 to 500 nm, and it fluoresces green when absorbing visible light.[18][15]

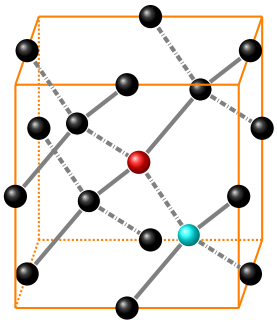

(e) Nitrogen-Vacancy center (NV) consisting of 1 Nitrogen atoms and 1 Vacancy.[19]

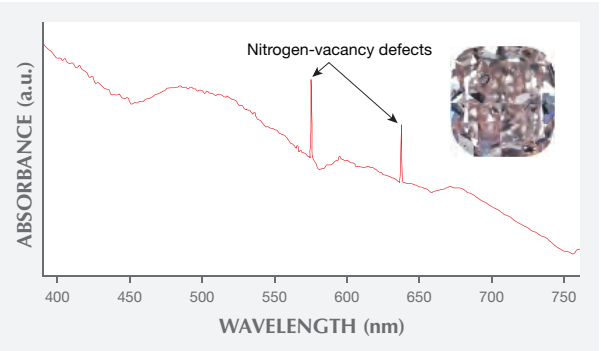

(f) NV absorbance spectrum with the NV^--line at 637 nm and the NV^0-line at 575 nm.[17][15]

Figure 4: A selection of Nitrogen-based defects in diamonds.

sensitive to the ion parameters such as especially speed / energy and direction, further mass and charge state. As a result, the ions do not get implanted in one specific location but rather a distribution of implanted particles emerges. If one were to trace the path of all implanted ions, then their shape would resemble the roots of a tree. Further, depending on the nature of the ions, they may kick out target atoms from their original position and thereby create vacancies or end up as interstitial atoms, or displace other target atoms themselves.

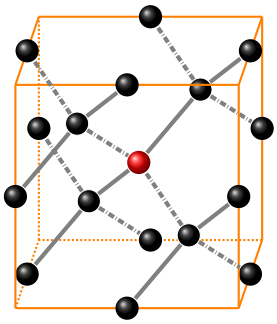

(a) GR1 defect consisting of 1 Vacancy.[18]

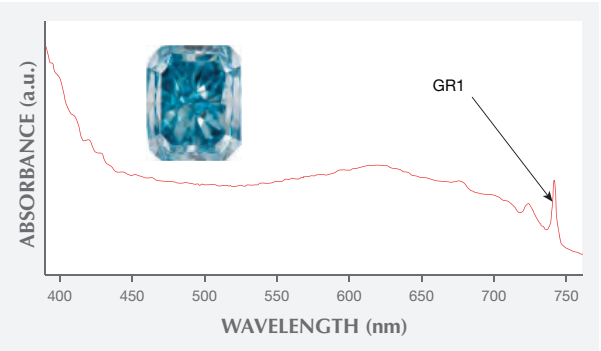

(b) GR1 absorbance spectrum with the GR1-lines at 740.9 nm and 744.4 nm, giving rise to a green or blue hue.[17][18][15]

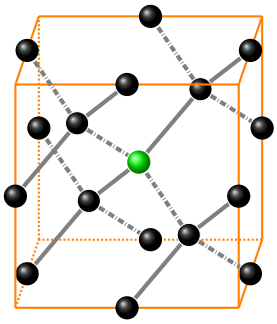

(c) Boron defect consisting of 1 substitutional Boron atom.[20]

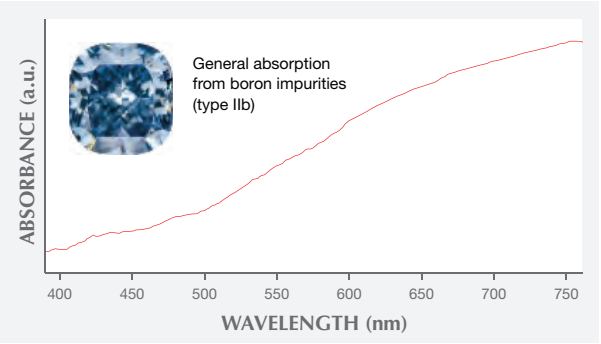

(d) Boron defect absorbance spectrum. There is also an IR line at 3.56 µm.[17][15]

Figure 5: A selection of other defects in diamonds.

In general, the more energy ions have, the deeper they travel into the target material. Light ions typically damage the target material near their final depth, whereas heavy ions deposit their energy, i. e. harm the material, closer to the surface due to nuclear collisions.

3 Experimental Methods

3.1 100kV Accelerator

The 100kV accelerator can be seen as it is *in situ* in figure 6. Its SNICS II ion source and general setup is described in more detail in figure 7 and in figure 8, respectively.

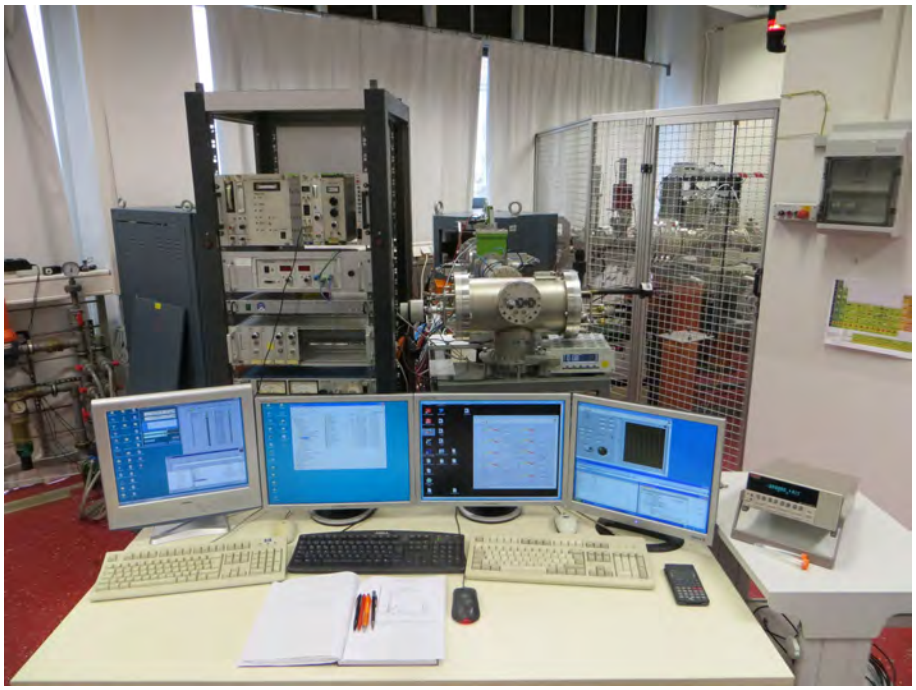

Figure 6: 100kV Accelerator in the Lab.[21]

The ion source SNICS II ("**S**ource of **N**egative **I**ons by **C**esium **S**puttering"), see figure 7, creates negative ions, i. e. anions. First, Cesium is vaporized in an oven (■) and subsequently flows into the chamber. Most of the atoms get positively ionized by the heated surface (■), referred to as the ionizer, in a process called thermal ionization. A negative voltage U_{Cat} of down to -10kV is applied to the cooled cathode (■) and its electric field accelerates the Cs^+ cations towards the cathode surface where they reduce to Cs^0 atoms and due to their kinetic energy they sputter particles from the implantation material (■) through the Cs^0 film. Due to Cesium's low electronegativity, i. e. large likelihood of surrendering electrons in a chemical reaction, the sputtered particles are favored to gain electrons and thereby become negatively charged. As a result the anions are accelerated back in the direction of the ionizer where the extraction voltage of the extractor U_{Ext} accelerates them into the beamline (■) with a voltage of up to 15kV.[23]

Upon extraction, the anions are accelerated further in a general purpose acceleration tube by U_{Lin} up to an additional 75kV, see figure 8.[25] Thereafter, a Faraday cup (■) can be placed pneumatically in or outside the beamline for a custom amount of time, using a computer program. Faraday cups are cup-shaped devices that can register a change of charge on their surface of known area during a certain amount of time and thus allow for a measurement of the ion current. If a Faraday cup is placed in the beamline, then it catches the entire beam and thus blocks off all ions from passing to the next elements of the implantation setup. Since it is possible to tune the Faraday cup such that it lets the

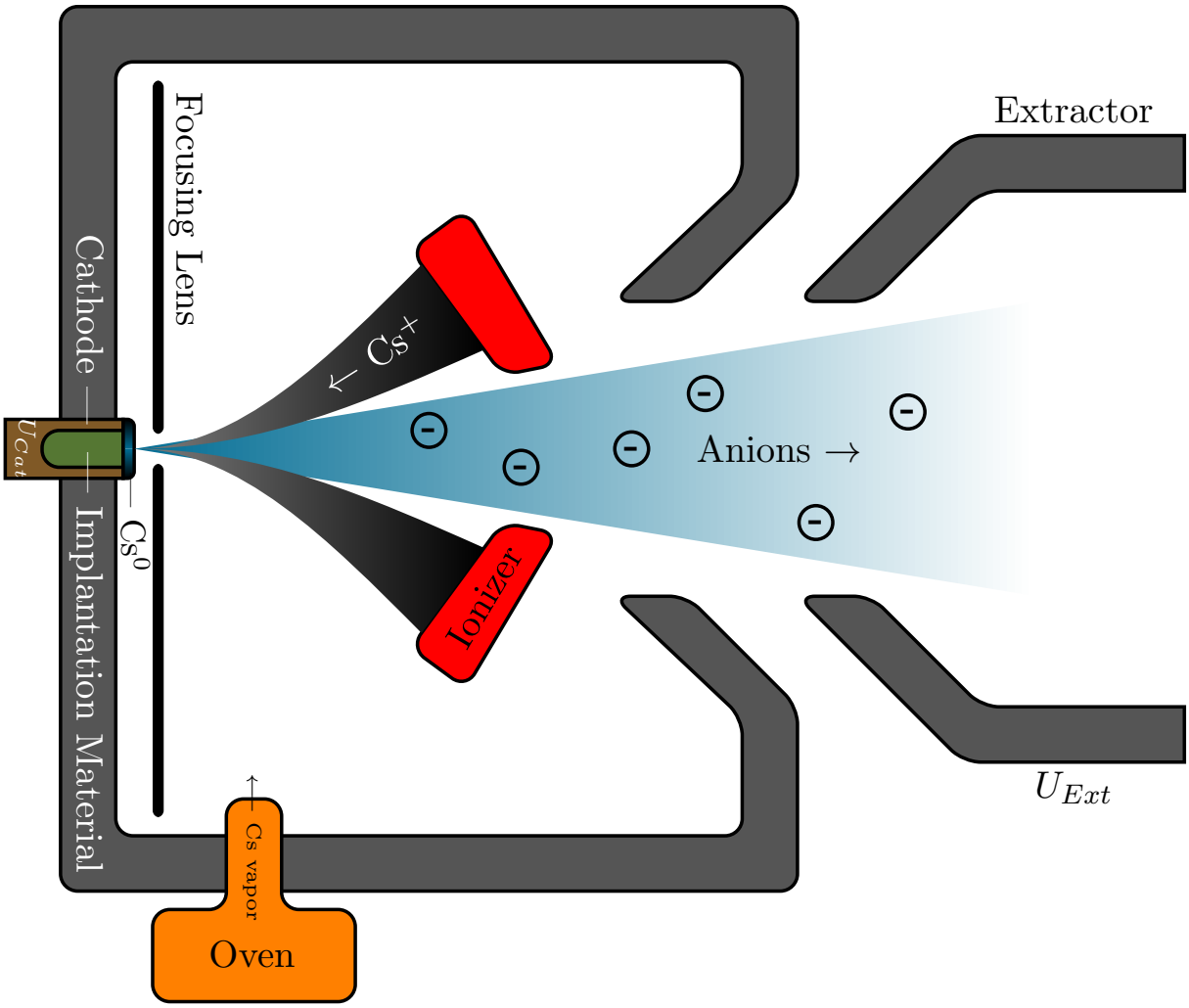

Figure 7: SCNICS II ion source.[22]

ions through for a specific time only, one can therefore set the number of particles that are to be used for the implantation into the sample. Valves 1 and 2 (■) can be used to close off parts of the accelerator for changing the sample or maintenance while preserving the vacuum in the rest of the setup.

The bending magnet (■) serves two purposes. First, it redirects the beamline to the rest of the implantation setup using the Lorentz Force $\mathbf{F}_L$:

$$\mathbf{F}_L = q\,(\mathbf{v} \times \mathbf{B}) \tag{1}$$

In the setup used here, the magnetic flux density $\mathbf{B}$ points out of the drawing plane towards the reader of figure 8 and the negative charge of the anions $q < 0$, together with their velocity v, result in a circularly bent beamline. Equation (1) also hints at the second purpose of the magnet: Mass spectrometry. In most applications of this setup, only one specific sort of particles shall be implanted. There are many possible contaminants in the beamline, whose origins may for example lie in an imperfect vacuum, Cesium from the ionizer or other particles from the cathode as it usually contains more than one sort of atoms or molecules. Therefore all but the type of particles one wishes to implant have to be filtered out of the beamline. Considering the setup, all particles ejected from the

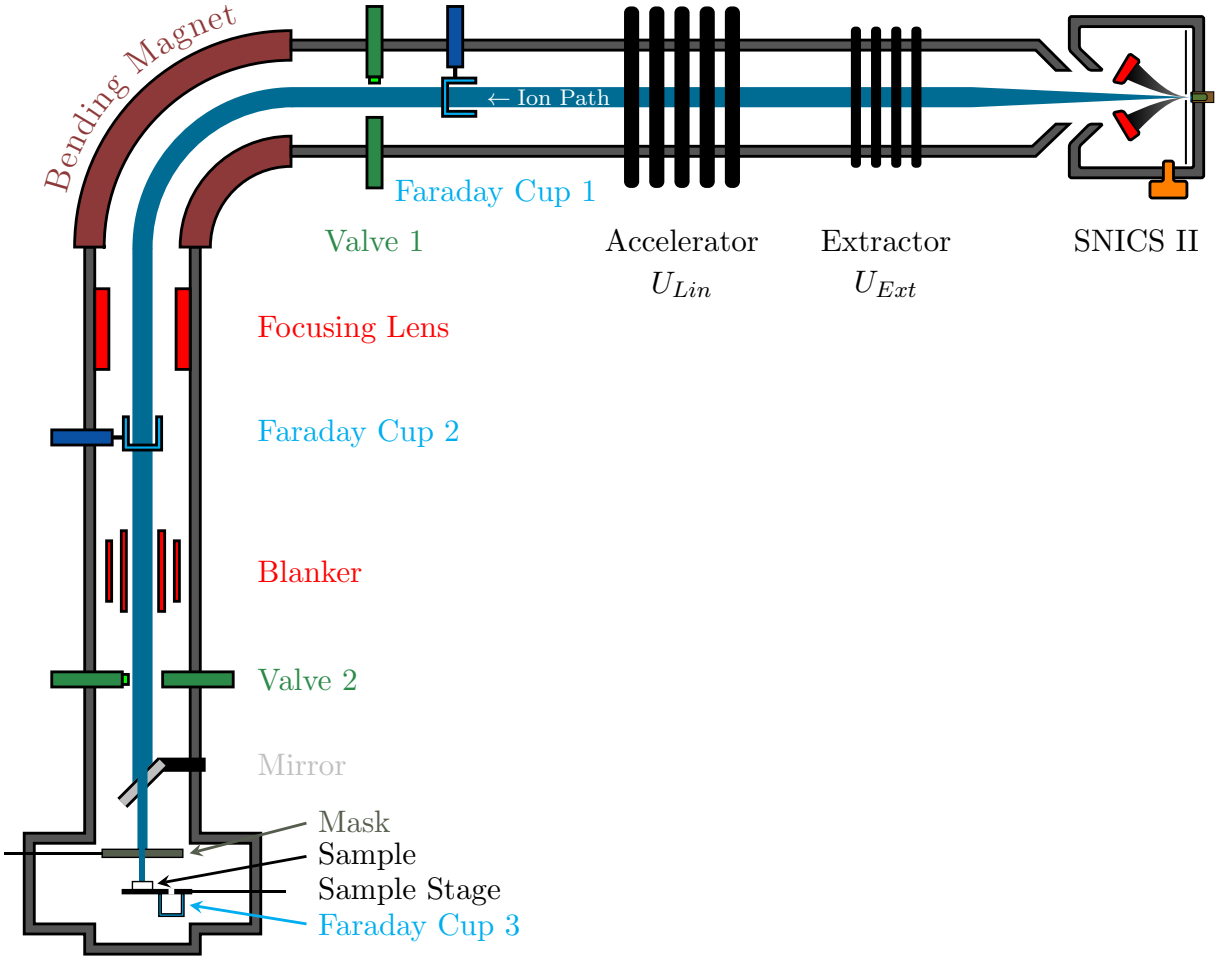

Figure 8: Main components of the electrostatic linear 100 kV accelerator setup.[24]

cathode are accelerated by the same high voltage U and thus their kinetic energies E_{kin} are equal:

$$E_{kin} = \frac{1}{2}mv^2 = qU \tag{2}$$

In theory, one could have multiply charged anions but in this experiment only single charged anions are implanted. Different kinds of particles have different masses m, so according to equation (2) their velocity will be different. Explicitly, their velocity will be:

$$v = \sqrt{\frac{2qU}{m}} \tag{3}$$

As long as the particles traverse through the homogeneous magnetic field of the bending magnets, the Lorentz force will stay the same and thus constrains the particles into a circular trajectory. The radius r of this trajectory is determined by the equilibrium between the Lorentz force, see equation (1), and the centripetal force $\mathbf{F}_Z$:

$$\mathbf{F}_Z = \frac{m\mathbf{v}^2}{r}\hat{\mathbf{r}} \tag{4}$$

From the equilibrium of forces (eq. (1) and (4)) the radius turns out to be:

$$r = \sqrt{\frac{2mU}{qB^2}} \tag{5}$$

Thence, the radius r changes for different masses m. However, by adjusting the magnetic flux density B one can adjust the radius to pick out any desired type of particle from the initial ion beam and keep them in the beamline while all other particles are thrown away. In order to know which magnetic flux density to use, Faraday cup 2 comes in handy. Before conducting the implantation, one records a mass spectrum, i. e. intensity vs. mass-to-charge ratio, by varying the magnetic flux density and simultaneously measuring the current into Faraday cup 2. Since all particles in the beamline are single negatively charged, the mass spectrum really is a intensity vs. mass graph. From the periodic table of elements one can determine the expected mass of the particle that is to be implanted. Because the radius is fixed in this setup, equation (5) can be rearranged to convert the magnetic flux density values into the mass values used for the mass spectrum:

$$m = \frac{qB^2r^2}{2U} \tag{6}$$

Choosing the magnetic flux density B now only amounts to selecting the desired mass on the mass spectrum and tune B in the vicinity of the peak to find the maximum current. In other words, selecting the mass m of the particles that are allowed to pass through is only a matter of changing B. The focusing lens (■) shown in figure 8 narrows the beamline and lets it converge on the sample.

Depending on the strength of the ion current and the desired amount of particles for the implantation, the required exposure time may sometimes be too short for the pneumatic apparatus of Faraday cup 1 to handle opening and closing accurately enough. This becomes especially relevant for exposure times below 2 seconds. In order to fix this, the blanker (■) is introduced. It is essentially an electrostatic octupole along the beamline that can rapidly divert the beam by generating electric fields $\mathbf{E}$ which exert a Coulomb force $\mathbf{F}_C$ on moving particles of charge q:

$$\mathbf{F}_C = q\mathbf{E} \tag{7}$$

Alternatively, one can also use the blanker to adjust the beamline constantly to maximize the ion current.

For the purpose of positioning the implantation mask (■) as well as the sample stage correctly, a camera is attached to the mirror (■), which has a hole in its center to let the beam pass through. Both the mask, which contains several differently shaped and sized holes, and the stage are mounted on step motors that allow movement in three dimensions on a micrometer scale. Attached to the sample stage is the sample, which the ions shall be implanted into, as well as a sheet of PMMA and Faraday cup 3. This third cup allows for a measurement of the current that is finally incident on the sample. It is also the one used to set the blanker and the position of the mask so that the current is maximal. This current is used to determine the exposure time, i. e. opening time, supplied to Faraday cup 1. The sheet of PMMA serves to validate both spatial accuracy and position of the

beam relative to the point of view of the camera.

In the configuration present in the lab, a maximum accelerating voltage gradient of in total 100kV is achievable, namely from $U_{Cat} = -10\text{kV}$ to $U_{Ext} + U_{Lin} = 90\text{kV}$. The maximal possible particle velocity for the lightest anion H^- is[1]:

$$v = \sqrt{\frac{2qU}{m}} \approx 4.37 \cdot 10^6 \ \frac{\text{m}}{\text{s}} \approx 0.015c \tag{8}$$

As it amounts only to about 1.5% of the speed of light, there are no relativistic corrections necessary for the purposes of this experiment.

3.2 Vacuum Furnace

The vacuum furnace depicted in figure 9 is used in this experiment to anneal the sample which allows a recrystallization of the diamond's constituent atoms and impurities where the implanted particles become a part of the new crystal lattice as defects. In order to prevent chemical reactions, e. g. combustion, of the sample with its environment during the heat treatment, the interior of the furance is connected to vacuum pumps that remove the air inside the oven. By raising the temperature of the furnace controlledly in small increments, the sample is given enough time to heat up thoroughly which prevents cracking of the surface through thermal expansion. Similarly during the cooling phase, the temperature is lowered in small decrements to avoid the very same. The duration of the heating at the final temperature may also be varied, depending on the sample under investigation.

Figure 9: Vacuum furnace in the Lab.[29]

[1] Elementary charge[26] $q = e \approx 1.60 \cdot 10^{-19}$ C, maximum voltage $U = 100$ kV, mass[27] $m \approx 1.67 \cdot 10^{-27}$ kg and speed of light[28] $c \approx 3.00 \cdot 10^8 \frac{\text{m}}{\text{s}}$.

The furnance itself consists of a cylindrical graphite cup functioning as the crucible of the furnance, surrounded by heating elements which are connected to a power supply. A layer of insulation around those elements keeps the heat inside and protects the exterior, while vacuum pumps remove the air inside.

3.3 Laser Lithography

The laser lithography setup enables a quasi printing of metallic structures with a theoretical resolution in the sub-micrometer range. In practice, however, the size of individual features is limited by the lift-off, as explained later. The lithography process begins with drawing the mask in a computer program, in this case the freeware LayoutEditor[30] was used. From there, the mask is imported into the computer at the lithography setup where one selects anchor points on the mask that define the scale and position on the sample. Before starting the lithography, one has to prepare the sample using a fine brush to apply a photoresist, in this case the negative "AZ nLOF 2020"[31], which is a viscous fluid consisting of a solvent and one or more types of monomers where exposure to certain wavelengths of light causes those to polymerize making them less soluble in the solvent. As will be described later, a developer solution as well as a stripper solution is necessary to remove the remaining liquid and keep the polymers in their place.[32] Depending on the sample size, surface tension tends to bulge the liquid, making the layer thicker in the center while the edges remain thinly coated. In order to even out the surface, the sample is placed onto a spin coater where the centrifugal forces arising from the fast rotation of the disc push the liquid to the edges of the sample. The general setup of this device is shown in figure 10.

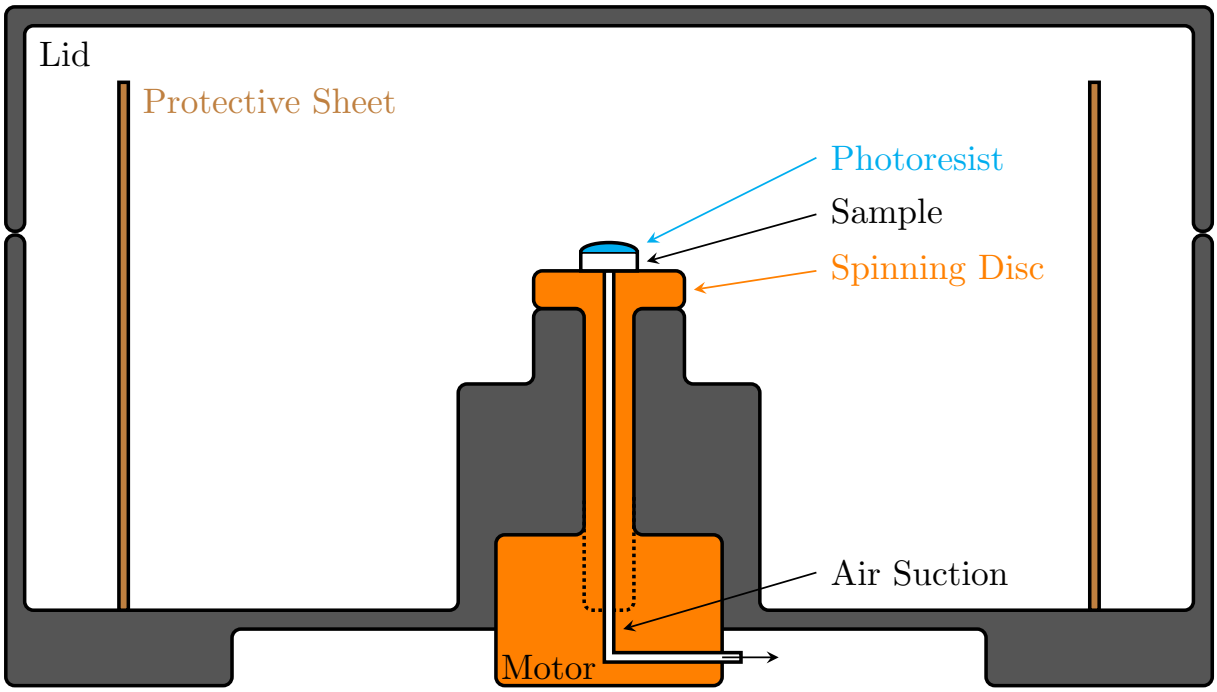

Figure 10: Main components of the spin coater setup.[33]

When idle, the lid of the spin coater is open to allow access to the spinning disc (■), upon which the sample, with its photoresist coating (■) on top, is put. The disc has a small hole in its center which locks the sample in place once the air suction is activated. A removable protective sheet of plastic (■) prevents splashes of photoresist liquid from contaminating the inner walls of the spin coater. When working with this apparatus, one has to balance the duration and speed of rotation so as not to throw too much of the coating off the sample but still manage to even it out enough so that it is usable for the next steps in the lithography process. For this experiment, a rotational speed of 6000 rpm for 25 s is used. In practice, the photoresist still turns out a little thicker at the edges than it is at the center of the sample. To lessen this effect, a spacing of around 10% of the sample dimensions was used between edges and beginning of the mask. The mask used here can be viewed in figure 22. Following this, the sample is put on a hot plate at 110 °C for 120 s.

Up next, the sample is placed on the carrier platform in the lithography machine, where it is clamped using an air suction. Two points on the self-designed digital lithography mask are now chosen as the anchor points to fix scale and orientation of the mask on the sample. Analogously to a regular printer, a print head, freely movable in the two dimensional plane and additionally adjustable in height for bringing the laser beam in focus, now illuminates the sample strip by strip in such a way that the beam follows the pattern of the mask. The laser applies a radiant exposure of $310\frac{\text{mJ}}{\text{cm}^2}$ at a wavelength of 405 nm. Following this, the sample is again put on a hot plate at 110 °C for 120 s. Now, the sample is dipped into a developer solution (Tetramethylammonium hydroxide, or TMAH) for about 40 s to remove the unpolymerized residue of the photoresist. Subsequently, the sample is dried in the spin coater at 6000 rpm for 25 s.

Under a microscope the edges of the lithographed mask are now visible. Using a sputter coater, the indentations of the pattern printed into the mask can then be filled with various different elements so that the desired structures form on the surface of the sample. The sputter coater is a hollow cylindrical chamber that, after placing the sample on a stage inside, is filled with Argon gas which becomes a plasma upon electron-impact ionization, where the Argon atoms form positively charged cations. Applying a voltage such that the disc of coating material, also called the target, at the roof of the chamber, which is attached to a magnetron that also supplies the electrons necessary for the Argon ionization, is negatively charged, this accelerates the Ar^+ ions to the target where they knock out uncharged target atoms which then fall down to the bottom, where the positively charged / grounded stage is located, onto the sample. In this process called sputtering, the entire sample surface gets covered, e. g. with Gold or Palladium. The duration of this procedure corresponds to the thickness of the metallic layer. During the experiment, it is advisable for the thickness of the photoresist to exceed the sputtered layer by a large amount.

Lastly, using a stripper solution, in this case "TechniStrip Ni555"[34], the remaining photoresist as well as the polymerized mask is removed in a process called lift-off. This happens by placing the sample in the stripper solution and heating it to 70 °C for over an hour. After taking the sample carefully out of the solution, one can cautiously scratch the unwanted pieces of metal off the surface using a very fine needle. This is easiest, when the sample is still wet from the solution. Lastly, using acetone and isopropyl acohol the surface can be cleaned. Now, the sample is ready for measurements.

3.4 Measurement Setup

In order to investigate the sample, a suitable measurement setup has to be developed. The one used in the experiments of this Bachelor Thesis can be viewed in figure 11. Since the desired data requires photocurrent measurements at a great variety of photon energies, i. e. wavelengths / colors, the best available light source is a white light laser. The light beam that it outputs is sent through a optical chopper to create light pulses. The chopper essentially consists of a spinning circular saw blade, where the light beam is placed such that the teeth of the blade alternatingly block and unblock the light. Combining the speed of rotation of the disc with the number and length of the saw teeth yields the duration of the blocking / unblocking of the light beam, i. e. the pulse length.

It is presumably preferable to use pulses instead of a continuous illumination because there is a certain duration in the process of exciting an electron from the valence to the conduction band and then refilling the hole that this creates with another electron supplied by the other side of the electric circuit. Also, using a pulse of a known time length allows for the use of a lock-in amplifier. The benefits of this tool will be outlined later.

The white laser light then goes through a monochromator, where it gets split up into its wavelength / color components. This can be implemented for example using refraction in a prism or diffraction in an optical grating. The desired wavelength is then extracted simply by placing a slit in the box wherever that part of the light lands. In the former case, the prism can be rotated to change the refraction angle and thereby the output direction of the light; in the latter case the grating can be moved to change the absolute output positions of the diffracted rays. If the measurement was not done using a mixed-color light source but a monochromatic light source, e. g. red-/green-/blue-colored laser, the monochromator is redundant but at the same time, each measurement at a different photon energy would require dismounting the previous light source and then mounting the next one. Hence, a mixed-color light source is simply more practical in this experiment.

Due to spatial limitations in the DLTS lab of the Semiconductor Physics Department, a parabolic mirror is used to redirect the now monochromatic light, as well as narrow the beam diameter. In order to focus the light to an even smaller spot size, a focusing lens (here: biconvex) was used. This is beneficial especially at low laser power, because the photons get bundled into a smaller area and do not illuminate spots of the sample where there is no implantation that is of interest for the current measurement.

The two ends of the electronic circuit on the sample stage, observable in figure 12, are connected to a pre-amplifier. The sample stage consists of a 3d-movable platform to which the circuit board, with the sample glued to it, is attached. The pre-amplifier supplies the bias voltage and amplifies the output signal of the current from the sample. The signal is then fed into a lock-in amplifier, from where it gets read out and recorded by a computer software. A lock-in amplifier can filter out noise very well by locking onto the periodic nature of the signal introduced by the chopper while all other frequencies that are present are filtered out. Quasi as a bonus, the lock-in amplifier also hands out phase data, which can give further information about the amplitude of the signal; in general, the phase is stable and close to zero when the signal is clear and contains little noise.

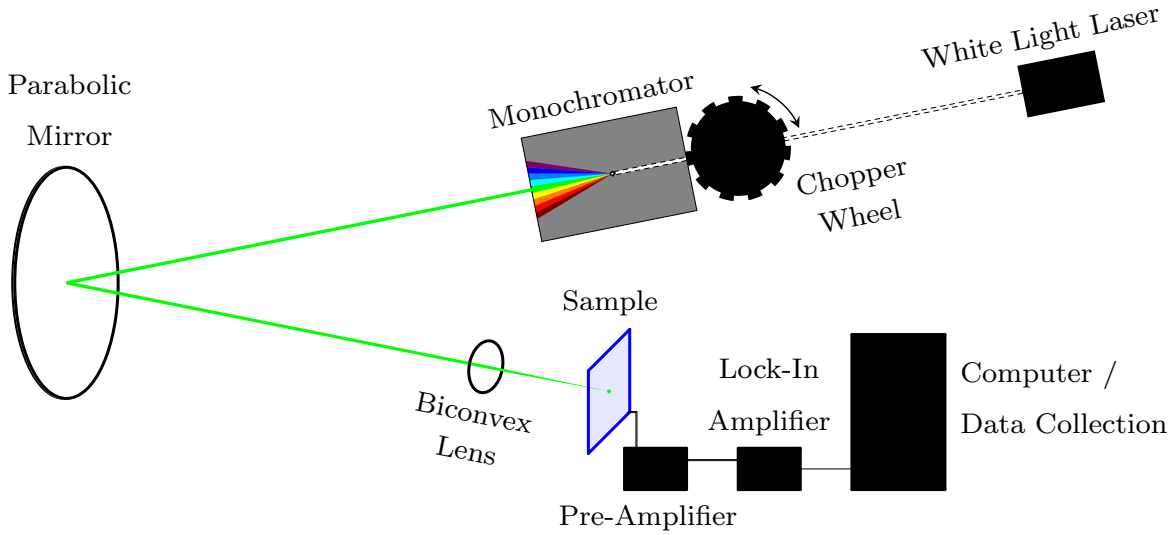

Figure 11: Schematic of the measurement setup.

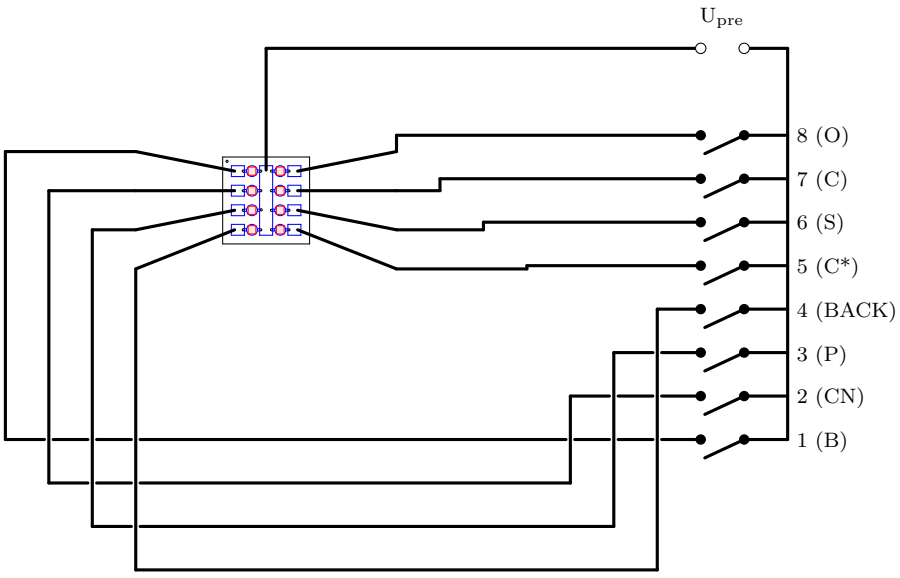

Figure 12: Schematic of the wiring on the sample stage between the implantation spots and the eight switches.

4 Experimental Implementation

4.1 Sample Preparation

4.1.1 Implantation

The program interface of the 100kV-accelerator only gives a few selectable mask sizes to choose from. In this experiment, the 180 µm × 200 µm option was selected, while a measurement of the resulting implanted spots came out to be approximately 179 µm × 189 µm in size. Thus, all specifications of implanted fluence, i. e. number of particles per area, (in the following simply referred to as "fluence" or Φ_{set}) have to be mask-corrected by a factor of 0.93975, or about 6%.

The implantation duration t_{imp} is calculated using the following equation:

$$t_{imp} = \frac{A_{mask} \cdot \Phi_{set}}{I_{set}} \tag{9}$$

In equation (9) the area of the selected mask[2] $A_{mask} = 3.6 \cdot 10^{-4}\text{cm}^2$ and the implantation current that is obtained from the particle accelerator I_{set} is introduced. Note that for simplicity only single-charge ions are of interest here, where $N = A_{mask} \cdot \Phi_{set}$ corresponds to the number of implanted ions. Hence, the current has units $\frac{1}{\text{second}}$. Further, I_{set} might not be entirely constant during the implantation. Assuming a linear change in the implantation current $I_{imp}(t)$ from the beginning of an implantation to its end, an estimate of the actual fluence Φ_{act}, i. e. mask- and current-corrected, can be made using measurements of the current right before the implantation (I_{set}) and thereafter (I_{act}) by deriving a fluence correction equation. The linearity assumption can be expressed as:

$$I_{imp}(t) = k \cdot t + I_0 \tag{10}$$

The slope k in (10) can be determined from the difference quotient to be $k = \frac{I_{act} - I_{set}}{t_{imp}}$, t corresponds to the time that has passed since the beginning ($t = 0$) of the implantation and I_0 is in this case equal to I_{set}.[3] The time integral of the implantation current yields the total number of particles that were implanted, so in order to obtain the acutal fluence the integral is divided by A_{mask}:

$$\Phi_{act} = \frac{1}{A_{mask}} \int_0^{t_{imp}} I_{imp}(t)\, dt = \frac{1}{A_{mask}} \left[\frac{1}{2} k \left(t_{imp}\right)^2 + I_0 \cdot t_{imp} + c_0 \right] \tag{11}$$

In equation (11), the "$+c_0$" can be omitted unless one has significant inaccuracies in the machinery that controls the fluence, e. g. in the implantation cup or the blanker of the accelerator. Recalling equation (9), the current-corrected fluence therefore turns out to be:

$$\Phi_{cur} = \left[1 + \frac{I_{act} - I_{set}}{2 \cdot I_{set}} \right] \cdot \Phi_{set} \tag{12}$$

Equation (12) still has to be adjusted for the error in the area of the mask. As described earlier, this can be done by multiplying Φ_{cur} with $n_{mask} \approx 0.94$, which is the mask

[2] $A_{mask} = 200 \cdot 10^{-6}\text{m} \cdot 180 \cdot 10^{-6}\text{m} = 3.6 \cdot 10^{-8}\text{m}^2 = 3.6 \cdot 10^{-4}\text{cm}^2$

[3] $I_{imp}(t = 0) = I_0$ and since by definition $I_{imp}(0) = I_{set}$, one obtains $I_0 = I_{set}$

correction factor.[4] Therefore, the fluence correction equation is:

$$\Phi_{act} = n_{mask} \cdot \left[1 + \frac{I_{act} - I_{set}}{2 \cdot I_{set}}\right] \cdot \Phi_{set} \tag{13}$$

If $I_{imp}(t)$ is not linear, then this approach can still be used, although one has to come up with another function to plug into equation (11). The values for Φ_{act}, as well as their devitation Δ from Φ_{set}, in tables 2 to 9 were rounded to three significant figures. Recall that due to the difference in mask size and the software, there is a baseline deviation of about -6.03%, however, the total Δ can vary depending on the ion current before and after the impantation. For every kind of ion, two different implantation energies E_I were used. The atomic masses are given according to the periodic table of elements[35] and the implantation energies as well as the fluences are mostly guided by T. Lühmann's dissertation[36]. Tables 2 to 8 display the implantation parameters and figures 13 to 18 show the depth distribution of the corresponding particles. These were simulated using the SRIM software[37]. For a better overview, table 9 gives the parameters in one combined table. The implantation layout of the sample is illustrated in figure 19.

Implantation Step		E_I [keV]	Φ_{set} [cm^{-2}]	I_{set} [pA]	I_{act} [pA]	Φ_{act} [cm^{-2}]	Δ [%]
$^{11}_{5}B^-$	№1	15.0	$2.00 \cdot 10^{12}$	77.0	77.0	$1.88 \cdot 10^{12}$	−6.03
$^{11}_{5}B^-$	№2	30.0	$3.80 \cdot 10^{12}$	77.0	77.0	$3.57 \cdot 10^{12}$	−6.03

Table 2: Implantation Parameters for Boron.

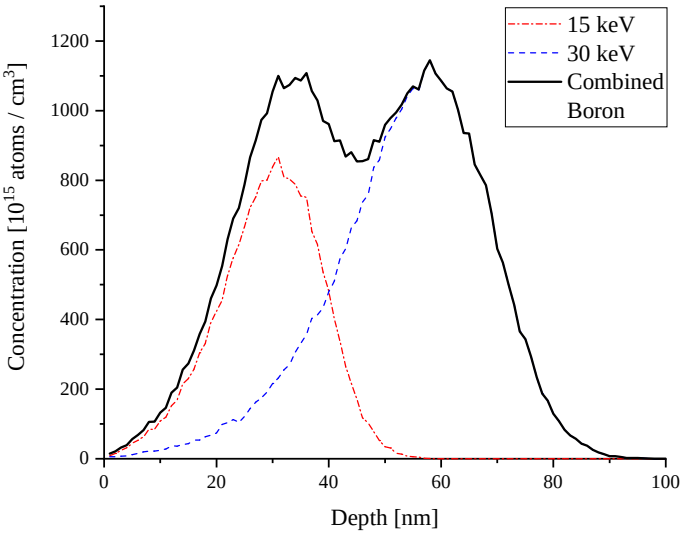

Figure 13: SRIM simulation of the Boron depth distribution concentration.

[4] $n_{mask} = \frac{189\ \mu m \cdot 179\ \mu m}{200\ \mu m \cdot 180\ \mu m} = 0.93975$

Implantation Step		E_I [keV]	Φ_{set} [cm^{-2}]	I_{set} [pA]	I_{act} [pA]	Φ_{act} [cm^{-2}]	Δ [%]
$^{16}_{8}O^-$	№1	25.0	$2.10 \cdot 10^{12}$	22.3	22.3	$1.97 \cdot 10^{12}$	−6.03
$^{16}_{8}O^-$	№2	50.0	$4.20 \cdot 10^{12}$	25.0	22.0	$3.71 \cdot 10^{12}$	−11.7

Table 3: Implantation parameters for Oxygen.

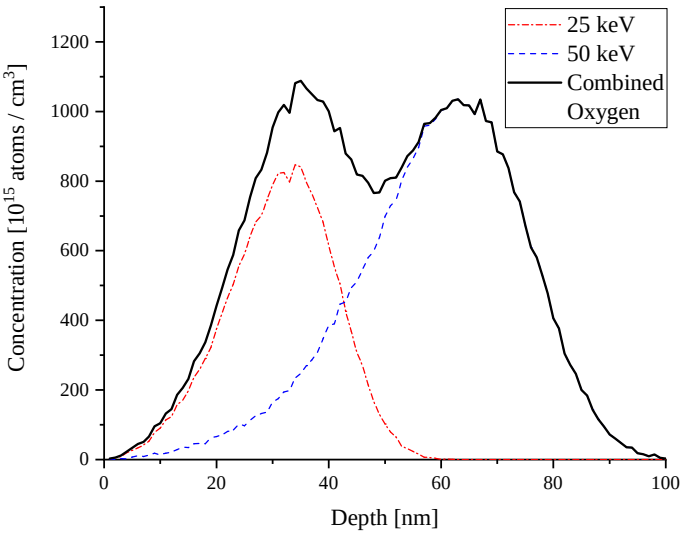

Figure 14: SRIM simulation of the Oxygen depth distribution concentration.

Implantation Step		E_I [keV]	Φ_{set} [cm^{-2}]	I_{set} [pA]	I_{act} [pA]	Φ_{act} [cm^{-2}]	Δ [%]
$^{26}CN^-$	№1	42.0	$2.10 \cdot 10^{12}$	6.30	6.50	$2.00 \cdot 10^{12}$	−4.53
$^{26}CN^-$	№2	84.0	$4.20 \cdot 10^{12}$	28.0	25.0	$3.74 \cdot 10^{12}$	−11.1

Table 4: Implantation parameters for the CN-molecule.

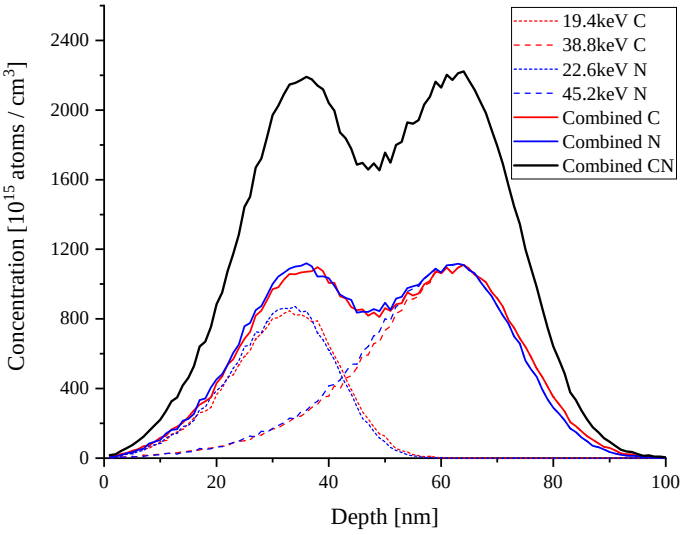

Figure 15: SRIM simulation of the CN-molecule depth distribution concentration.

Implantation	Step	E_I [keV]	Φ_{set} [cm^{-2}]	I_{set} [pA]	I_{act} [pA]	Φ_{act} [cm^{-2}]	Δ [%]
$^{12}_{6}C^{-}$	№1	19.5	$2.10 \cdot 10^{12}$	38.0	38.0	$1.97 \cdot 10^{12}$	−6.03
$^{12}_{6}C^{-}$	№2	39.0	$4.20 \cdot 10^{12}$	24.5	24.5	$3.95 \cdot 10^{12}$	−6.03

Table 5: Implantation parameters for Carbon (annealed).

Implantation	Step	E_I [keV]	Φ_{set} [cm^{-2}]	I_{set} [pA]	I_{act} [pA]	Φ_{act} [cm^{-2}]	Δ [%]
$^{12}_{6}C^{-}$	№1	19.5	$2.10 \cdot 10^{12}$	31.0	31.0	$1.97 \cdot 10^{12}$	−6.03
$^{12}_{6}C^{-}$	№2	39.0	$4.20 \cdot 10^{12}$	145	145	$3.95 \cdot 10^{12}$	−6.03

Table 6: Implantation parameters for Carbon (not-annealed).

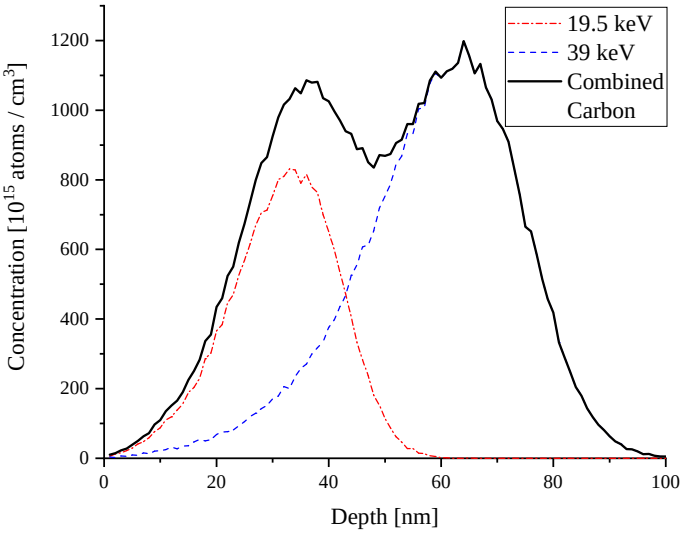

Figure 16: SRIM simulation of the Carbon depth distribution concentration.

Implantation	Step	E_I [keV]	Φ_{set} [cm^{-2}]	I_{set} [pA]	I_{act} [pA]	Φ_{act} [cm^{-2}]	Δ [%]
$^{31}_{15}P^{-}$	№1	40.0	$1.80 \cdot 10^{12}$	33.0	33.5	$1.70 \cdot 10^{12}$	−5.31
$^{31}_{15}P^{-}$	№2	80.0	$4.14 \cdot 10^{12}$	47.0	47.8	$3.92 \cdot 10^{12}$	−5.23

Table 7: Implantation parameters for Phosphorus.

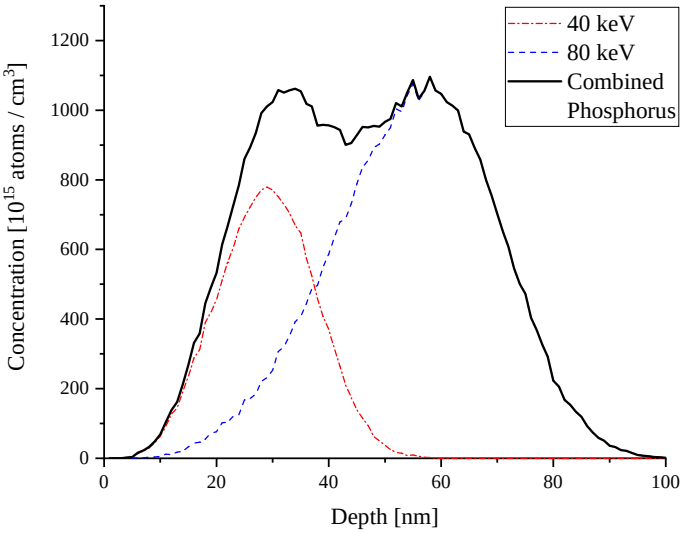

Figure 17: SRIM simulation of the Phosphorus depth distribution concentration.

Implantation Step		E_I [keV]	Φ_{set} [cm^{-2}]	I_{set} [pA]	I_{act} [pA]	Φ_{act} [cm^{-2}]	Δ [%]
$^{32}_{16}S^-$	№1	40.0	$1.60 \cdot 10^{12}$	54.5	56.0	$1.52 \cdot 10^{12}$	−4.73
$^{32}_{16}S^-$	№2	80.0	$3.70 \cdot 10^{12}$	23.5	25.5	$3.63 \cdot 10^{12}$	−2.03

Table 8: Implantation parameters for Sulphur.

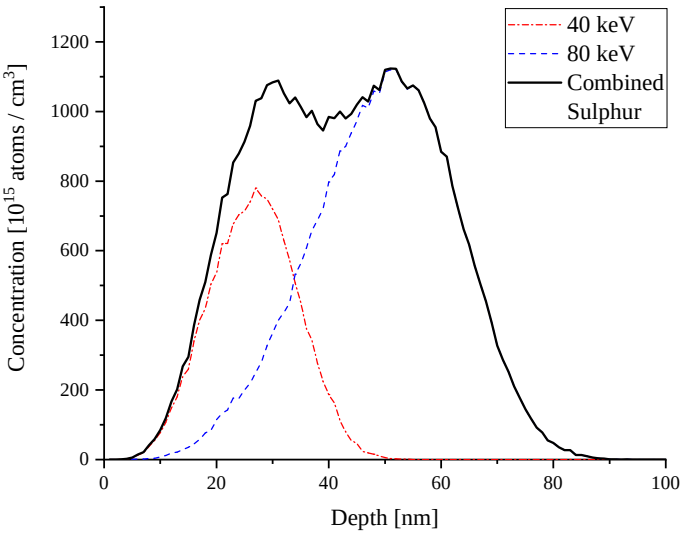

Figure 18: SRIM simulation of the Sulphur depth distribution concentration.

Implantation Step		E_I [keV]	Φ_{set} [cm^{-2}]	I_{set} [pA]	I_{act} [pA]	Φ_{act} [cm^{-2}]	Δ [%]
$^{11}_{5}B^-$	№1	15.0	$2.00 \cdot 10^{12}$	77.0	77.0	$1.88 \cdot 10^{12}$	−6.03
$^{11}_{5}B^-$	№2	30.0	$3.80 \cdot 10^{12}$	77.0	77.0	$3.57 \cdot 10^{12}$	−6.03
$^{16}_{8}O^-$	№1	25.0	$2.10 \cdot 10^{12}$	22.3	22.3	$1.97 \cdot 10^{12}$	−6.03
$^{16}_{8}O^-$	№2	50.0	$4.20 \cdot 10^{12}$	25.0	22.0	$3.71 \cdot 10^{12}$	−11.7
$^{26}CN^-$	№1	42.0	$2.10 \cdot 10^{12}$	6.30	6.50	$2.00 \cdot 10^{12}$	−4.53
$^{26}CN^-$	№2	84.0	$4.20 \cdot 10^{12}$	28.0	25.0	$3.74 \cdot 10^{12}$	−11.1
$^{12}_{6}C^-$	№1	19.5	$2.10 \cdot 10^{12}$	38.0	38.0	$1.97 \cdot 10^{12}$	−6.03
$^{12}_{6}C^-$	№2	39.0	$4.20 \cdot 10^{12}$	24.5	24.5	$3.95 \cdot 10^{12}$	−6.03
$^{31}_{15}P^-$	№1	40.0	$1.80 \cdot 10^{12}$	33.0	33.5	$1.70 \cdot 10^{12}$	−5.31
$^{31}_{15}P^-$	№2	80.0	$4.14 \cdot 10^{12}$	47.0	47.8	$3.92 \cdot 10^{12}$	−5.23
$^{32}_{16}S^-$	№1	40.0	$1.60 \cdot 10^{12}$	54.5	56.0	$1.52 \cdot 10^{12}$	−4.73
$^{32}_{16}S^-$	№2	80.0	$3.70 \cdot 10^{12}$	23.5	25.5	$3.63 \cdot 10^{12}$	−2.03
$^{12}_{6}C^{-*}$	№1	19.5	$2.10 \cdot 10^{12}$	31.0	31.0	$1.97 \cdot 10^{12}$	−6.03
$^{12}_{6}C^{-*}$	№2	39.0	$4.20 \cdot 10^{12}$	145	145	$3.95 \cdot 10^{12}$	−6.03

Table 9: Combined table of the implantation parameters. $^{12}_{6}C^{-*}$: $^{12}_{6}C^-$ not-annealed.

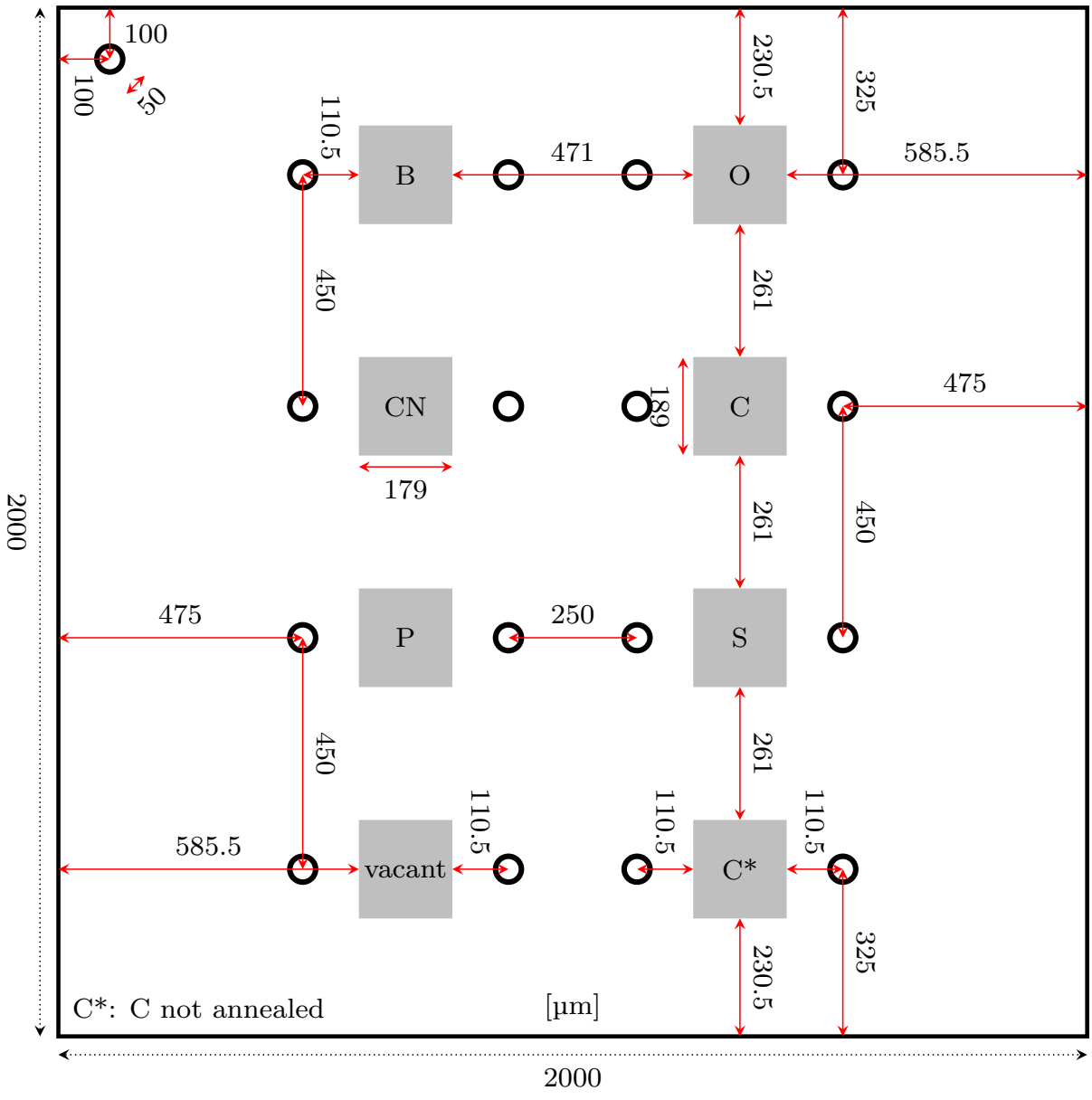

Figure 19: Implantation layout of the sample and the various implantation spots.

4.1.2 Annealing

The temperature curve that was set for annealing is shown in figure 20. Experimentally, the cooling phase may differ from the instructed settings the closer the system gets to room temperature because the cooling process is not aided by an external cooling device, meaning the rate at which the sample radiates off thermal energy slows down as the system approaches thermal equilibrium with its environment. Thus, in practice the temperature curve decreases not linearly but, especially at the very end, approaches room temperature asymptotically, i. e. slower than the linear instructed curve would predict.

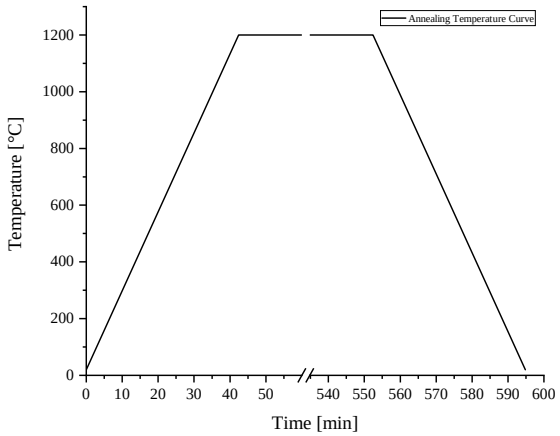

Figure 20: Temperature curve of the annealing process.

As depicted in figure 20, the total duration of the annealing spans about 9 hours and 55 minutes of which $8\frac{1}{2}$ hours are at the maximum annealing temperature. The heating phase takes approximately 42 min and the cooling phase extends for the same duration. The sample is placed in the oven for the entire process, even during the heat-up phase.

4.1.3 Laser Lithography

Getting the lift-off right is the most difficult part of the laser lithography. In total, it took three tries to obtain a satisfying result. The sample can be seen before and after the lithography with subsequent lift-off in figure 21. The lithography mask is shown in figure 22. After pre-sputtering (without the sample being exposed to the material) for 120 s at 60 W, Palladium was sputtered for 35 seconds at 60 W onto the sample. This results in a film with a thickness of about 100 to 150 nm. The first two tries with a Titanium and Gold film on top did not yield a usable coating, likely because the Titanium had an oxidized layer. In order to rule out any electrical shorts, the very sensitive Palladium coating has to be touched with thin needles, to which a multimeter is attached, and measured for any currents between all combinations of the contacts on the sample, especially with the edges of the sample. Afterwards, the contact pads of the Palladium coating (large rectangles visible in figure 21 (b)) have to be connected to the corresponding switches.

(a) Before lithography.

(b) After lithography.

Figure 21: Sample before and after the lithography and subsequent lift-off. For the mask design, see figure 22.

Using silver conductive paint, thin gold wires are glued to the contact pads and to the contacts of the switches on the sample stage. The result is shown in figure 23. Now, again, the sample has to be checked for any electrical shorts that could have been introduced by the glue, especially if it touches the edge of the sample. If the sample works properly, then there is no current between contacts, only within one contact.

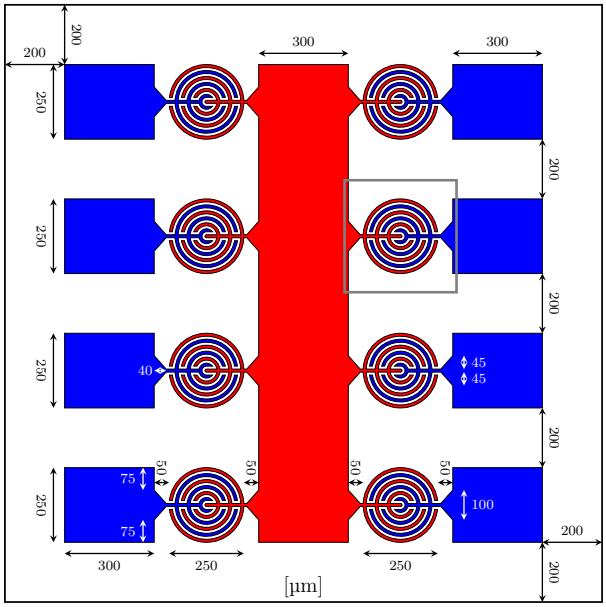

(a) Lithography Mask.

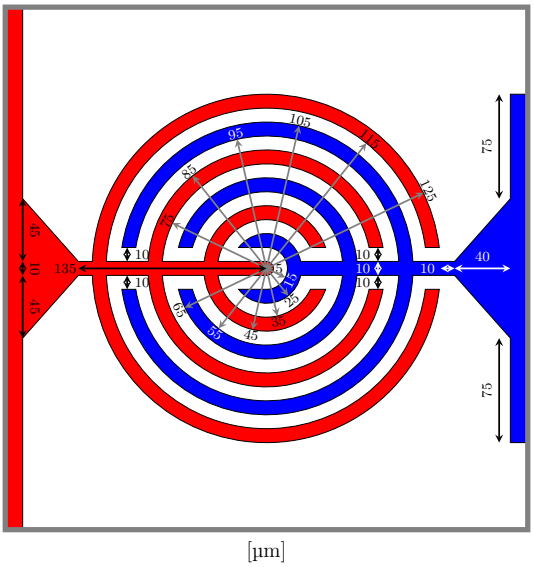

(b) Zoom-in on lithography Mask.

Figure 22: Lithography mask design for the 2000 × 2000 µm sized diamond.[38]

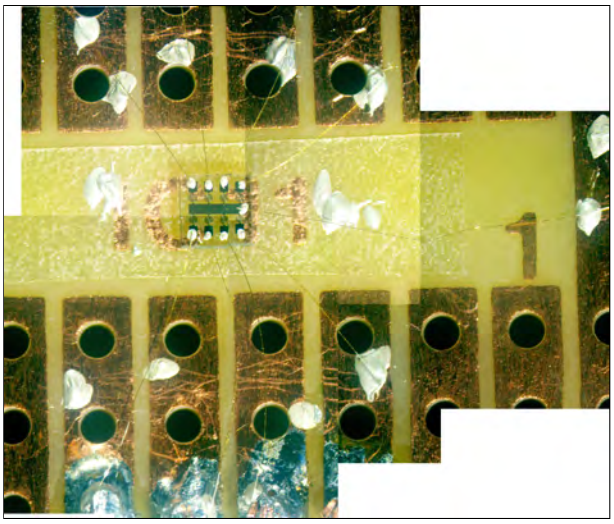

Figure 23: Diamond sample after connecting the contacts and gluing it to the stage.

4.2 Measurement Setup

The setup was constructed as discussed in section 3.4. In figure 24, some photos are shown of the sample stage. Experimentally, it is advantageous to check the output of the pre-amplifier without any input using an oscilloscope, before taking the measurements. That is because there can be systemic noise frequencies in the output signal of the pre-amplifier, for example the power grid operates at 50 Hz and in the oscilloscope, connected to the pre-amplifier, a peak can be observed at that point, as well as at multiples of that. Further, other components of the internal circuitry of the pre-amplifier can introduce other inherent noise frequencies to the output signal, and if their amplitude is large enough, then the lock-in amplifier might lock onto the noise signal instead of the measurement signal if the chopper frequency is in the vicinity of one of these noise frequencies. So, it is advisable to choose a chopper frequency where the pre-amplifier output spectrum does not have any major disturbances.

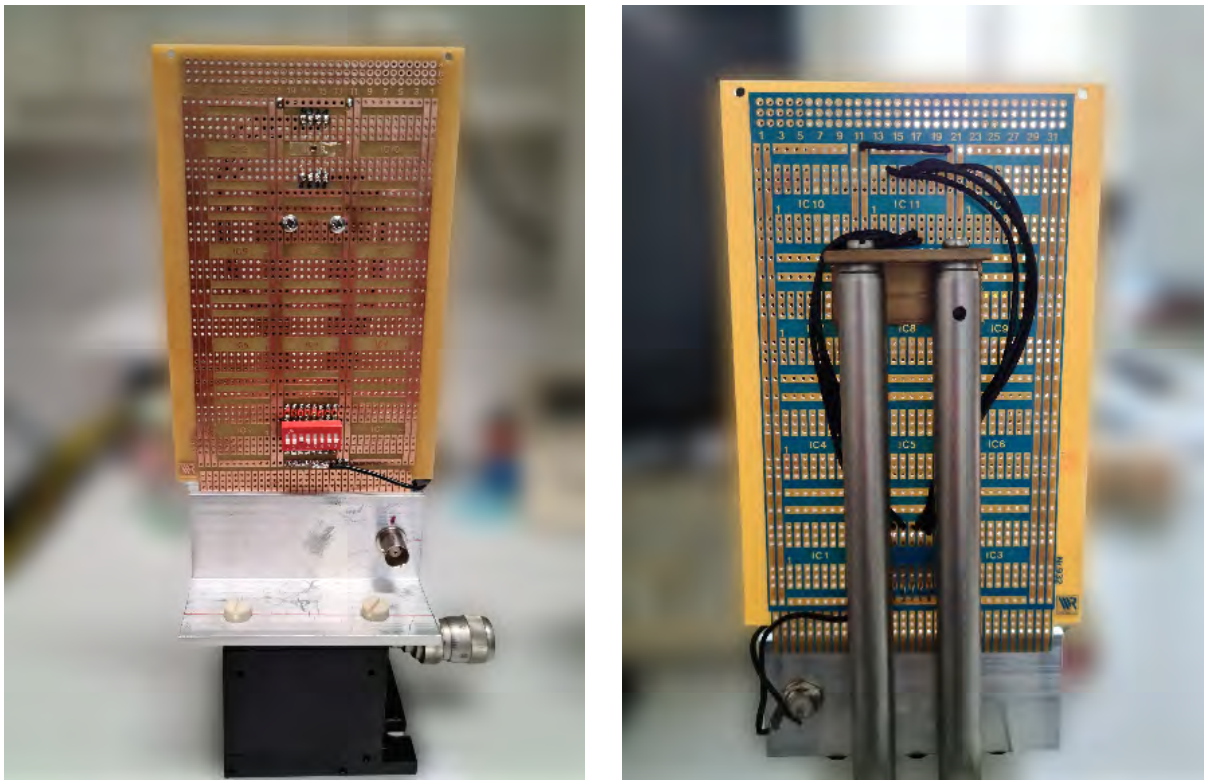

(a) Front view.

(b) Back view.

Figure 24: Photos of the sample stage.

5 Results and Discussion

5.1 Measurements

5.1.1 Laser Power Distribution and Diamond Background

For later analysis, recording the laser power distribution over the range of wavelengths that are going to be used is of immense importance. This distribution is called reference, or reference line. Especially when trying to identify peaks in the photocurrent spectra, it can be useful to compare raw data and normalized data. Here, normalized data means dividing each value of the raw data by the corresponding value of the reference line. This allows for a judgement whether a peak in a photocurrent spectrum stems from the sample itself or is just a result of the laser power being unusually large at that wavelength. The laser power distribution is shown in figure 25 with the markings of the three major peaks at 1.14, 1.62, 1.92 eV; and the two major troughs at 1.41, 1.74 eV. Unfortunately, the power ranges quite widely over three orders of magnitude, from 10^0 to 10^3 µW which may lead to some defects not being measured due to a lack of laser intensity and/or the measurement device not being sufficiently sensitive.

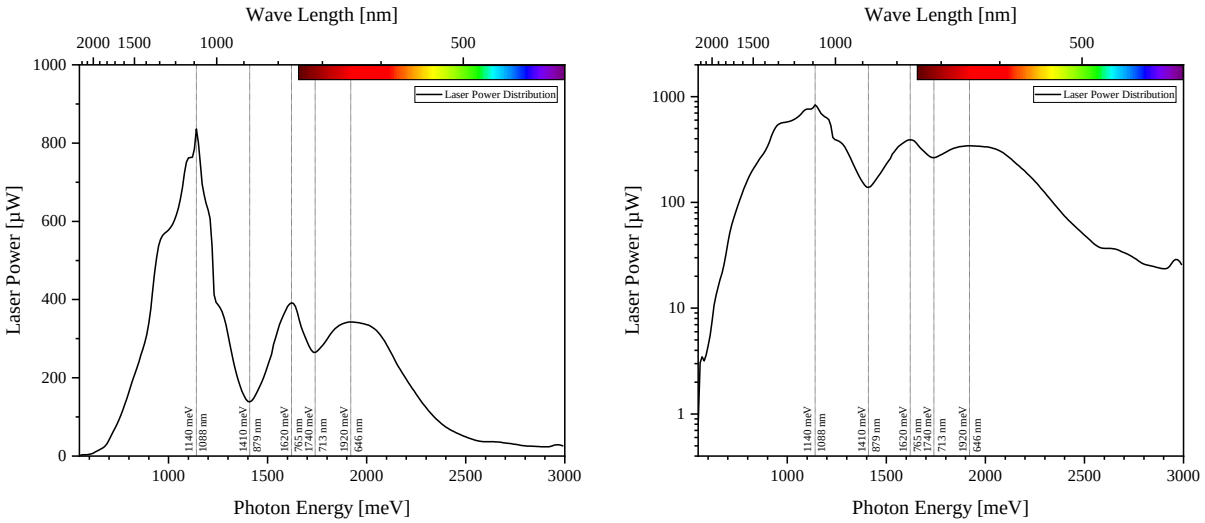

(a) Linear scale.

(b) Logarithmic scale.

Figure 25: Laser Power Distribution (sometimes also called reference line).

On the other hand, as can be seen later, the low laser power from 550 to 800 meV, around 1400 meV, and from 2300 to 3000 meV makes it very easy for normalized data to show a peak there since the denominator (reference spectrum) for these values is very small. For example: If the raw data was simply constant, then the normalized data will show the inverse of the reference spectrum. This means it will be difficult to distinguish between real peaks in photocurrent and artifacts created by the normalization. One way to reduce this effect in the judgement is to compare raw data and normalized data and decide accordingly.

Next, applying a bias voltage of $U_{pre} = 5$ V at the terminals of the sample stage, see figure 12, a photocurrent spectrum of the diamond without any additionally implanted ions can be measured, sometimes referred to as background or vacant spectrum. The resulting diagrams can be seen in figure 26 (a) and (b), where each graph contains the measurement as well as the reference line for a better comparison. Further, figure 26 (c) and (d) display the reference adjusted data ("Ref. Adj."), i. e. normalized — as explained above.

In the normalized diagrams of the background measurement in figure 26 it seems that there are several peaks below 750 meV but these do not appear in the raw data which means they spawn probably only due to the low laser power in this region and are therefore artifacts. Moving to higher energies, there are two bands in the linear graphs of the raw data ranging from 1110 to 1230 meV, with a peak at 1150 meV, and from 1360 to 1410 meV, with its peak at 1380 meV. The former essentially matches the reference peak at 1140 meV and hence disappears in the normalized diagram. The latter, however, remains and it is noteworthy that this second peak band is in a region where the reference spectrum has a trough but still shows up in the raw data. Before jumping to the conclusion that this is indeed a peak, it might be worth looking at the absolute magnitude of the photocurrent there which is 1.14 fA at the maximum (1380 meV). That is just barely above what seems to be the noise range from 0 to 1 fA. A more powerful laser would likely shed light on whether this peak can be considered real or not. Lastly, the most significant feature of the background data from figure 26 is the exponential increase in photocurrent starting in the raw data around 2290 meV and growing to about 4.30 fA. It is remarkable as well by how much the noise is reduced at this point, compared to lower energies where the data is much more volatile. In order to determine the starting point of the photocurrent more systematically, the measured phase will be considered.

As described in section 3.4, the phase is tends to zero when the registered signal becomes more stable, i. e. has less noise. Now, the recorded phase can range from $-180°$ to $+180°$ and arbitrarily defining a range of $\pm 10\%$ of that, meaning $\pm 18°$, as the tolerated deviation from zero phase angle for the photocurrent signal to be considered stable, yields a quantitave – although arbitrary – way of identifying real photocurrent peaks. In principle, this would be a sufficient criterion, however if there is even just a single artifact in the data, then one peak could be falsely identified as two peaks. One way to improve this procedure is using a moving average of n periods, this essentially smoothens the data by calculating the average of the values from the $(i - n)$-th index to the $(i + n)$-th index for all indices i. The trade-off here is the inaccuracy of the thereby determined starting point of the photocurrent. This method is not a sufficient criterion for identifying photocurrent peaks, but a necessary one. It is best to search for peaks in the raw data and then confirm them using the moving average. For example, the moving average in figure 26 (f) temporarily drops below the $\pm 18°$ threshold around 2150 meV, but neither the raw data nor the normalized data show a peak that goes above the surrounding noisy data at that energy. Thus, this suspected peak can be discarded.

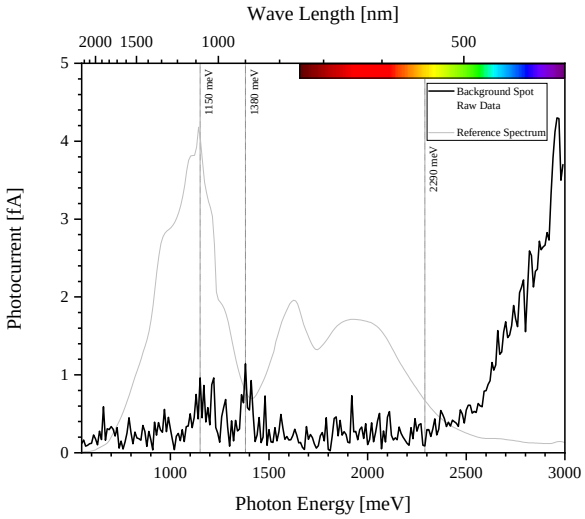

(a) Raw data, linear scale.

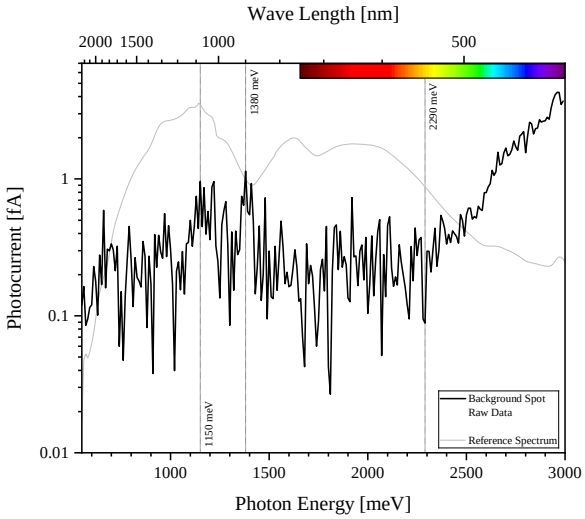

(b) Raw data, logarithmic scale.

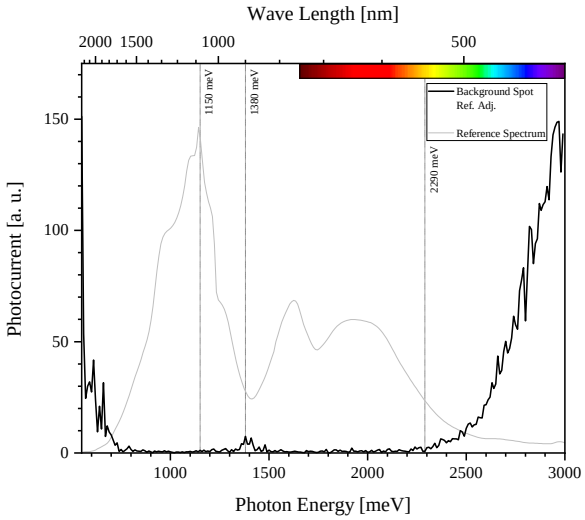

(c) Normalized data, linear scale.

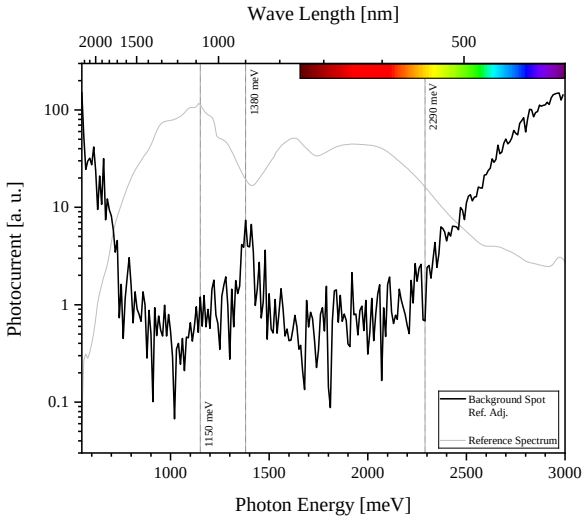

(d) Normalized data, logarithmic scale.

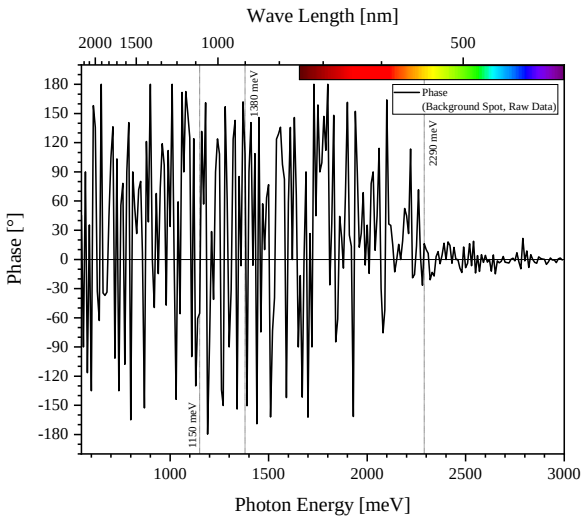

(e) Phase angle of background signal.

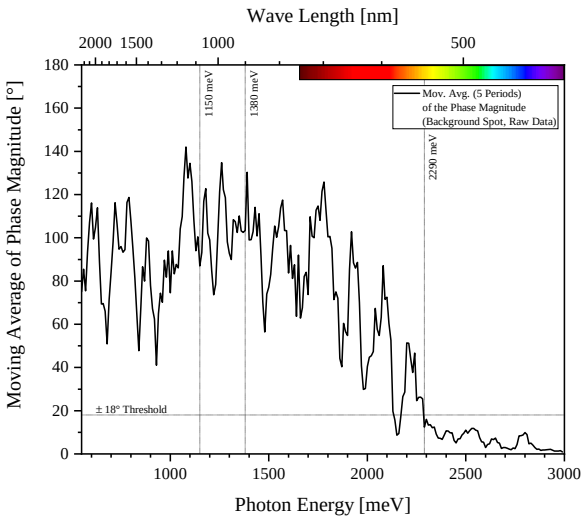

(f) Moving Average of phase, 5 periods.

Figure 26: Photocurrent spectrum of the diamond sample background without any additionally implanted ions, also called background spot. Bias voltage is 5 V. Phase data is given as well.

5.1.2 Boron

For the Boron spot, two different measurements were taken: One with a bias voltage of 2 V and one with 5 V. The results of these are shown in figures 27 and 28. The most striking difference between the background spot (see figure 26) and the Boron spot is the maximum photocurrent that was recorded. At the background spot, it amounts to approximately 4.30 fA, while for Boron the apex is at around 10.3 fA. Even the 2 V measurement grows to ca. 4.95 fA, which cannot directly be compared to the background measurement due to the difference in bias voltage, as the background was recorded at 5 V, but it underlines the conclusion that the spectrum obtained from Boron differs vastly from the background.

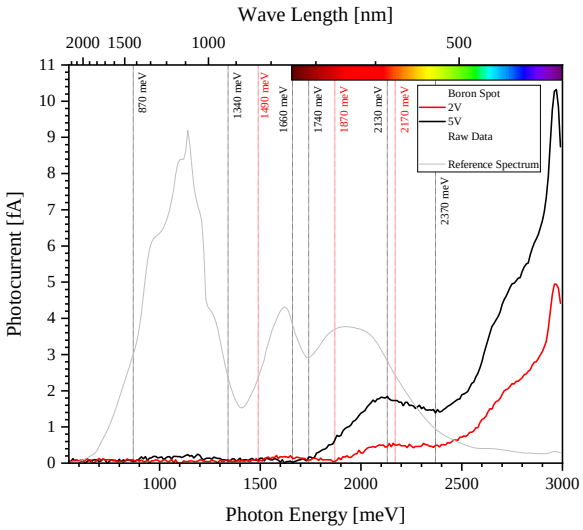

(a) Raw data, linear scale.

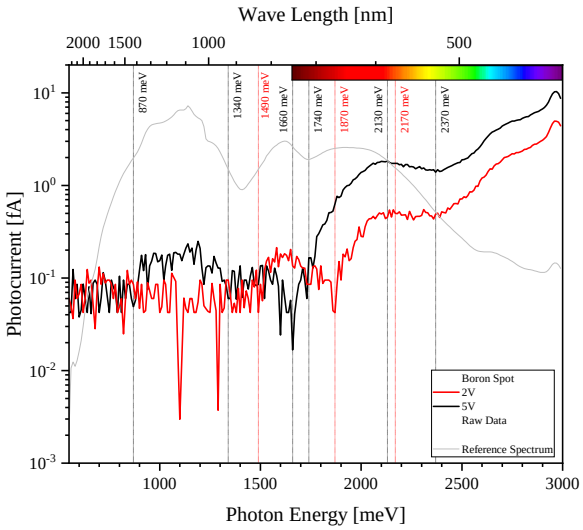

(b) Raw data, logarithmic scale.

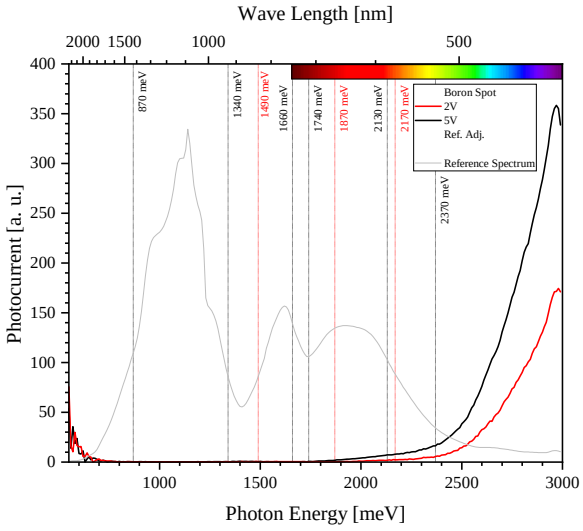

(c) Normalized data, linear scale.

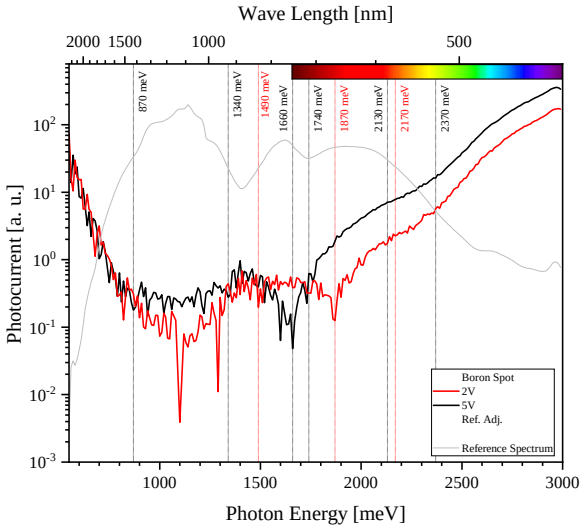

(d) Normalized data, logarithmic scale.

Figure 27: Photocurrent spectrum of the diamond sample at the Boron implantation spot. Bias voltage is 2 and 5 V, respectively. For phase data, see figure 28.

Further investigating figure 27 (a) and (b), the disparity between the 2 and 5 V measurement becomes evident, as there is a shift of the energies at which the photocurrent signal starts. Going by the moving-average-method as described in section 5.1.1, it commences

at 2170 meV for 2 V and at 1740 meV for 5 V, as marked in figure 28 (c). A more discretionary estimate could consider the dips to the left of these starting points in figure 27 (b) as better characterizations of the Boron spectrum. These would then be at 1870 meV for 2 V and 1660 meV for 5 V, which is 13.8% and 4.60% smaller, respectively. This deviation cannot unambiguously be calculated for the background, too, since there is not such a distinct trough right where the signal starts.

As a sidenote, comparing figure 27 (d) and (b) illustrates very well that not every peak in the normalized data stems from a peak in the raw data, as the raw data is more or less constant in the low energy range, while solely looking at the normalized data would suggest a peak at an energy below 550 meV, which is where the measurement range starts. This occurs because the laser power is so low there that the fraction of raw data to laser power, which is the definition of normalized data here, is comparatively high and decreases as the laser power increases, all while the raw data remains approximately unchanged.

Focusing on another discrepancy in the data, there seems to be another interval with a signal in the raw data, namely the band from 1490 to 1870 meV peaking at 1580 meV with 0.21 fA for a bias voltage for 2 V, while a similar band can be found in the 5 V data from 870 to 1340 meV with its maximum at 0.25 fA for 1190 meV. Oddly, these bands lie in the vicinity of the reference peaks at 1140 and 1620 meV, but do not turn up in *both* Boron spectra. Perhaps the two bands in the raw data are in fact the same but affected by the very shift in energy that the starting point of the signal has experienced, but given the starting points of the moving-average-method, the shift in energy from the 5 V to the 2 V data amounts to about +24.7% while the middle points of the bands shift by ca. +52.0%, which is more than double that, i. e. this does not seem to be the case. Together with the amount of current at these bands' peaks being even lower than what was considered noise in the background in section 5.1.1, see figure 26, makes that hypothesis unlikely and suggests that these two bands are not meaningful and can be disregarded.

An explanation of the shift between the two bias voltages possibly rests in the laser power distribution. Recalling that it lies in the microwatt range, the intensity might simply be too weak to create a measurable photocurrent. One way to counteract this is to increase the bias voltage since that makes it easier for the electrons that transition to the conduction band to be carried through the circuit and thereby get recorded. As a consequence of this argument, illuminating one spot with photons of the same wavelength should yield a higher photocurrent for higher bias voltages which is corroborated by the data as in figure 27 (a) and (b). The photocurrent dependence on the bias voltage is looked into in more detail in section 5.1.8.

In the raw data of the Boron spectrum, there is also a drop in photocurrent in the interval from approximately 2130 to 2370 meV. In the 5 V data, this drop of about 24.5% from maximum to minimum is more pronounced than in the 2 V data where it is rather a stagnation. In contrast to the apparently different starting points of the photocurrent signal, this feature is situated at roughly the same energies. Comparing it to the reference spectrum, the point at which the laser power starts to decrease exponentially coincides with the aforementioned interval. The normalized data of figure 27 (c) and (d) hints at the laser distribution being the reason for the drop in the raw data as well.

Next, subtracting the normalized background data from the normalized Boron data, which will be called background adjusted data or "Ref. Adj., Backgr. Adj." in the diagrams, yields a starting point of the photocurrent at about 1840 meV, which is about 5.74% larger than what the moving-average-method found above. The corresponding graph is shown in figure 28 (a). The starting point is defined here as the last crossing point of the zero-current line. The background data was collected only with a bias voltage of 5 V, so it cannot be applied to the 2 V Boron data. Calculating this background adjusted data might reveal insights into splitting up the photocurrent into its background- and implantation-component, i. e. which portion of the photocurrent comes from the diamond sample and which portion is contributed by the Boron ions implanted into the diamond. The two other features in this diagrams, namely the negative bands at the low energy end of the range and at 1380 meV originate from the normalization and the background noise.

Lastly, the raw phase data in figure 28 (b) needs to be addressed. Similarly to figure 26 (e), it is quite jumpy at energies below the starting point of the photocurrent signal, meaning it is essentially just noise. However, there are two anomalies in the Boron data that are not visible in the background data. In the range from 910 to 1210 meV, the 5 V phase seems to be fairly stable. If there was a real signal, then the lock-in amplifier should read out a phase angle of (close to) zero degrees. While briefer, this interval nonetheless falls into the one described above from 870 to 1340 meV, located around the first reference spectrum peak. Likewise in the 2 V phase, a phase stabilization occurs from 1440 to 1550 meV which is shorter than the abovesaid 2 V band from 1490 to 1870 meV, but it might be worth noting that the phase in circumambient energies switches between close to $+180°$ and $-180°$ a lot, which implies that this phase stabilization might actually be more extended but is not recognizable here due to the phase being recorded in the $\pm 180°$ format rather than ranging from $0°$ to $360°$. However, this paragraph does not infer that these bands are indeed a relevant signal, but based on this data it cannot entirely be ruled out either. Further studies in this energy range with more measurements at different bias voltages and a more stable or powerful laser could clarify this issue.

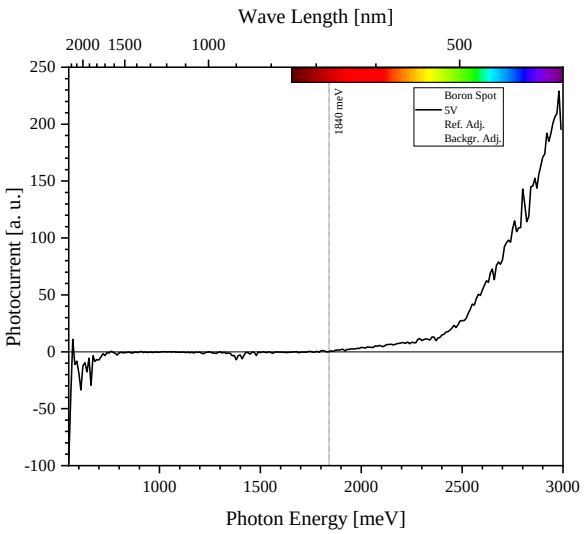

(a) Normalized and background adjusted, linear scale.

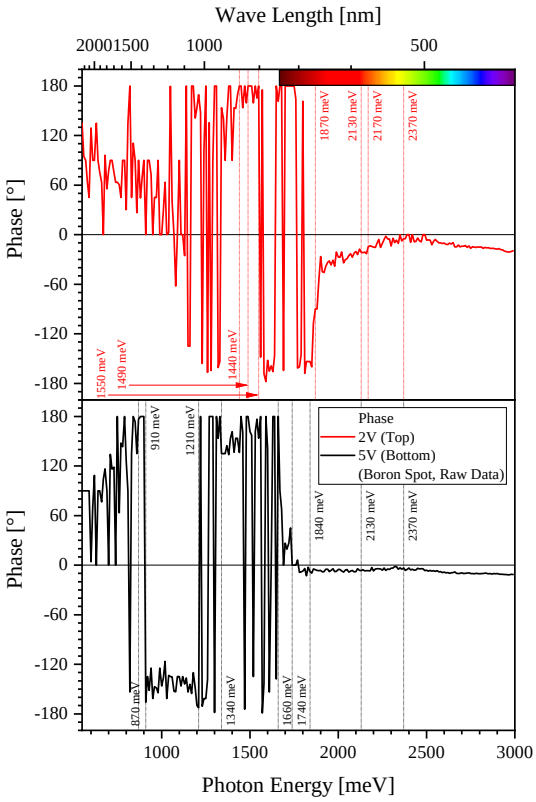

(b) Phase angle of Boron signal.

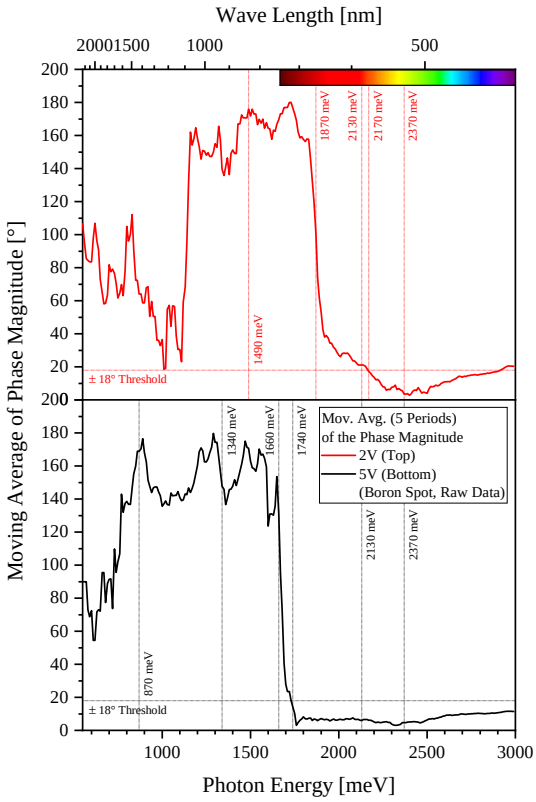

(c) Moving Average of phase, 5 periods.

Figure 28: Background adjusted data and phase data for the measurements from figure 27.

5.1.3 Phosphorus

For the Phosphorus spot, one data set was recorded with a bias voltage of 5 V. Plots of this data are displayed in figures 29 and 30. Proceeding with the analysis similarly to section 5.1.2, the first aspect to be looked at is the overall magnitude of photocurrent obtained in this measurement which is at most ca. 8.68 fA at 2970 meV. That is lower than Boron at approximately 10.3 fA but still more than double the background 4.30 fA. Also, the photocurrent starting point of 2030 meV, as determined by the moving-average-method, see figure 30 (c), differs from Boron at 1740 meV and the background at 2290 meV. Likewise, defining the starting point as in the previous section using the last trough before increasing exponentially, see figure 29 (a) and (b), it turns out to be about 11.3% less at 1800 meV, while that of Boron is at 1660 meV.

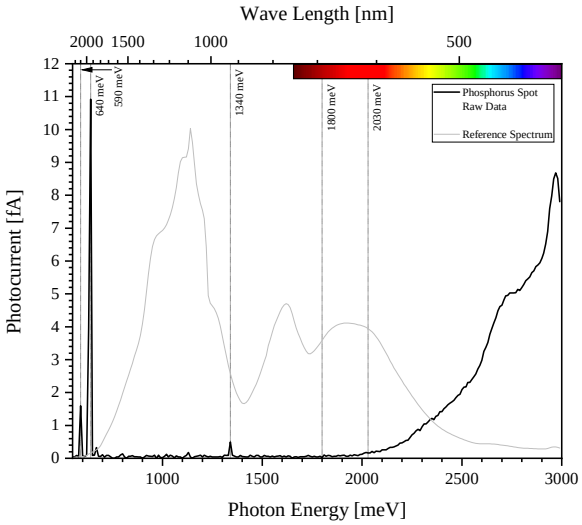

(a) Raw data, linear scale.

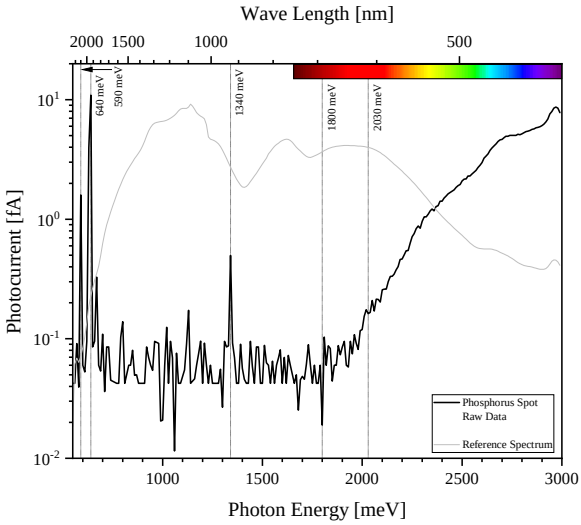

(b) Raw data, logarithmic scale.

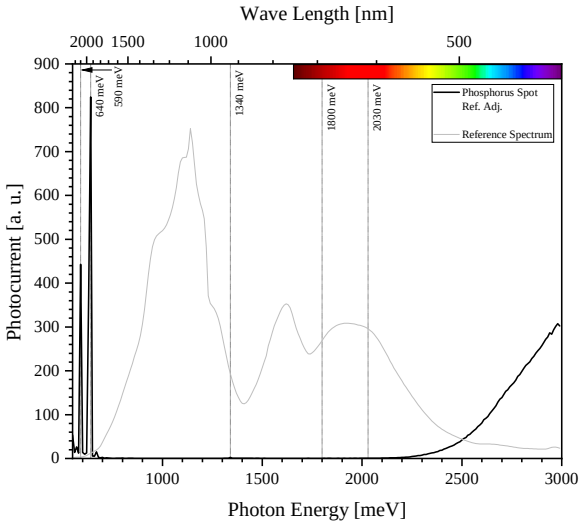

(c) Normalized data, linear scale.

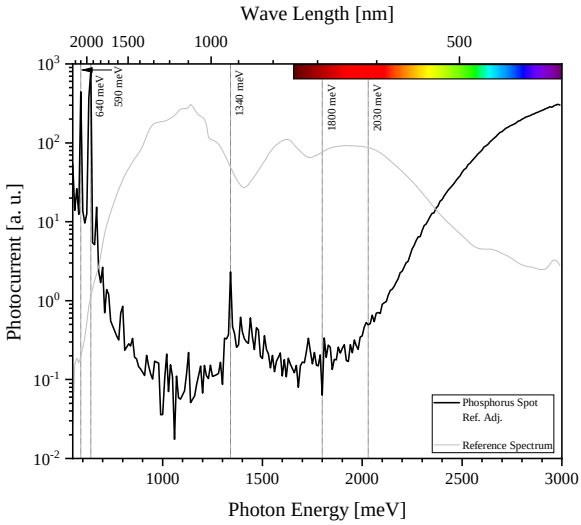

(d) Normalized data, logarithmic scale.

Figure 29: Photocurrent spectrum of the diamond sample at the Phosphorus implantation spot. Bias voltage is 5 V. For phase data, see figure 30.

Other than that, there are three other features in the plots of figures 27 (a) to (d) that are worth noting: Three peaks at 590 meV, 640 meV and 1340 meV. The latter attains a maximum of ca. 0.498 fA and, corroborated by the phase being fairly unstable as shown in figures 30 (b) and (c), can be labelled as an artifact or noise. These phase plots also suggest that the two other peaks can be considered noise as well. The one at 590 meV rises to about 1.59 fA, but recalling that the 1.14 fA peak at 1380 meV from the raw data as shown in figure 26 (a) and (b) was deemed noise, it does not seem too far fetched to label this peak as noise as well, especially considering that it consists of only one data point. The other peak mentioned above, namely that at 640 meV, attains its highest point at 10.9 fA which is even higher than the recorded maximum of the photocurrent signal which hits approximately 8.68 fA at the maximum. As a passing remark, this feature is constituted of not one but two data points deviating from the ambient noise level (the second data point is at 630 meV with ca. 3.96 fA). However, looking at the phase data in figures 30 it seems highly likely for this peak to be just another artifact.

The third way of determining the photocurrent starting point, as described in section 5.1.2, is to adjust the normalized data for the diamond background which then results in a plot shown in figure 30 (a). Here, the starting point turns out to be at 2120 meV, about 4.43% larger than the value obtained from the moving-average-method.

On a final note, barring the two artifacts at the low energy end, it noteworthy how smooth the Phosphorus data appears, particularly the normalized data shows effectively no bumps in the photocurrent signal region. In addition, the raw data of the phase is almost exclusively in the positive realm and hence much more concentrated than it was the case for the background and Boron.

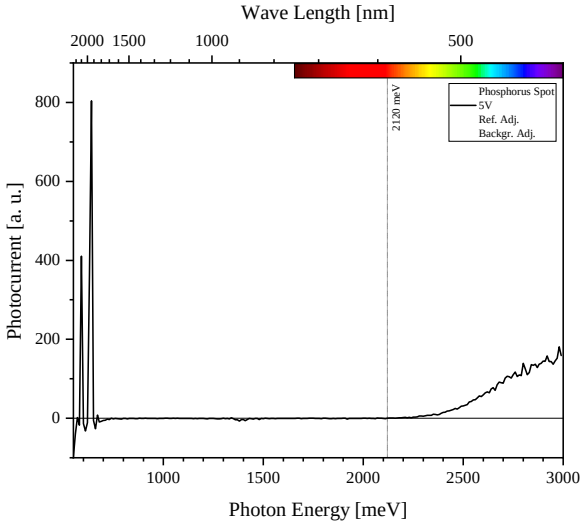

(a) Normalized and background adjusted, linear scale.

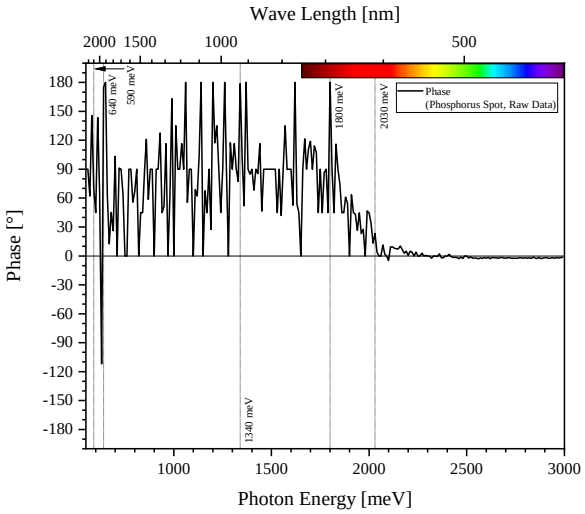

(b) Phase angle of Phosphorus signal.

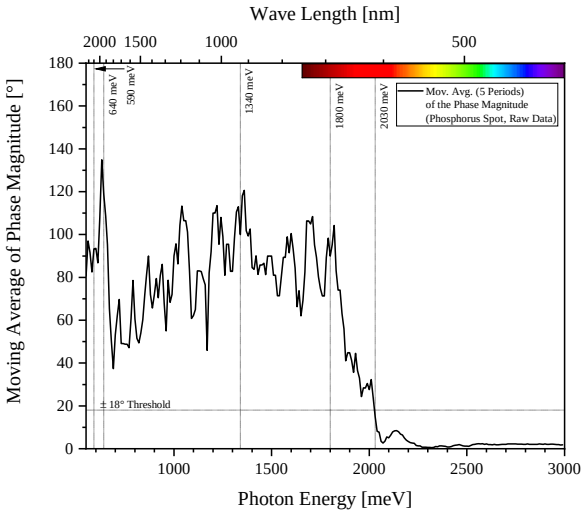

(c) Moving average of phase magnitude, 5 periods.

Figure 30: Background adjusted data and phase data for the measurements from figure 29.

5.1.4 Oxygen

For the Oxygen spot, four data series were measured at bias voltages of 0, 1, 2 and 5 V, one for each, respectively. These are plotted in figures 31, 32 and 33. The largest photocurrent is recorded at 2960 meV (0 V at 2950 meV) and it peaks at 0.267, 2.46, 3.74 and 5.81 fA for 0, 1, 2 and 5 V respectively. Comparing the 5 V measurement, this maximum is higher than the background (4.30 fA) but lower than both Boron (10.3 fA) and Phosphorus (8.68 fA).

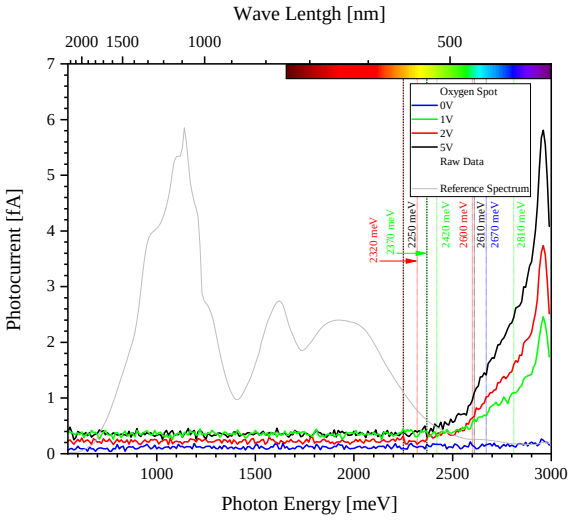

(a) Raw data, linear scale.

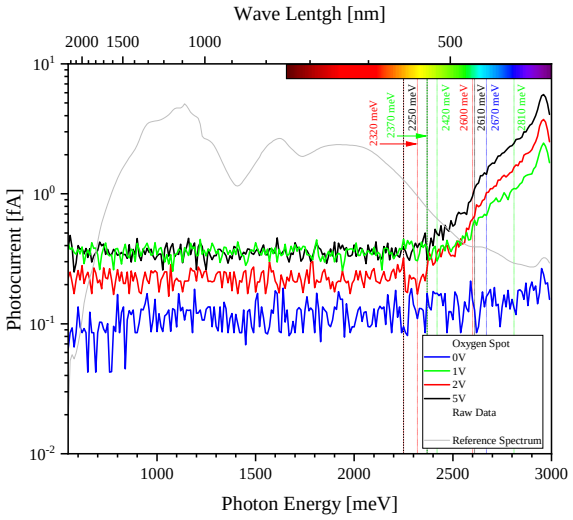

(b) Raw data, logarithmic scale.

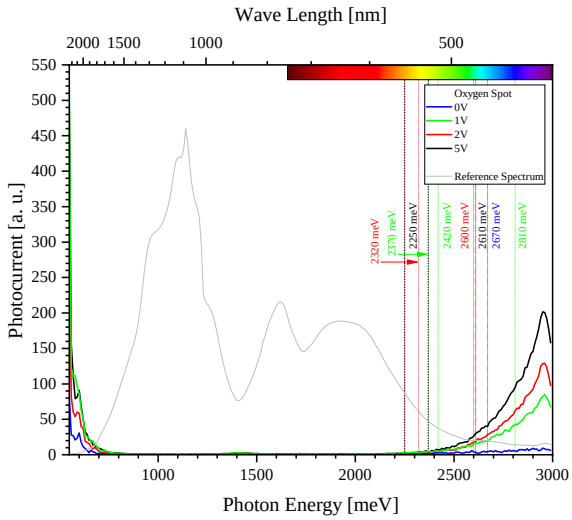

(c) Normalized data, linear scale.

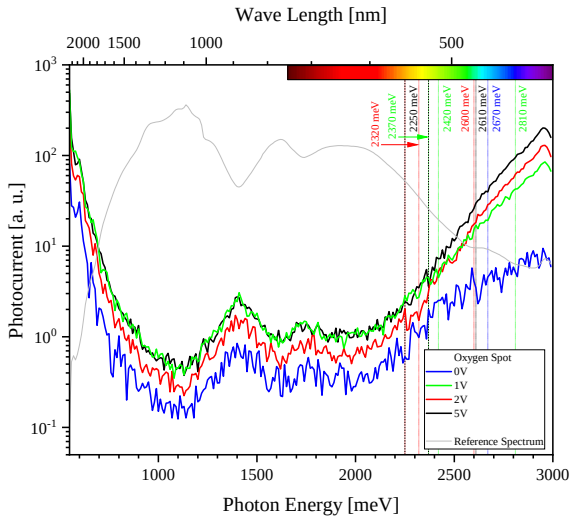

(d) Normalized data, logarithmic scale.

Figure 31: Photocurrent spectrum of the diamond sample at the Oxygen implantation spot. Bias voltage is $0, 1, 2$ and 5 V. For phase data, see figure 33.

The moving-average-method sets the photocurrent starting points at 2810, 2600 and 2610 meV for the 1, 2 and 5 V data, respectively. For the 0 V measurement, however, it does not return any starting point because somehow the phase data, see figure 33, does not converge to zero like in the other three measurements. Defining the starting point as the last trough similarly to the previous sections, the commencement of the photocurrent is

placed at 2420, 2320 and 2370 meV for 1, 2 and 5 V, respectively. Again, due to the small signal of the 0 V data, it is not obvious where to put the starting point, even in a discretionary way. In this data, even the maximum of 0.267 fA is well inside the noise range used in the analysis of previous implantation spots.

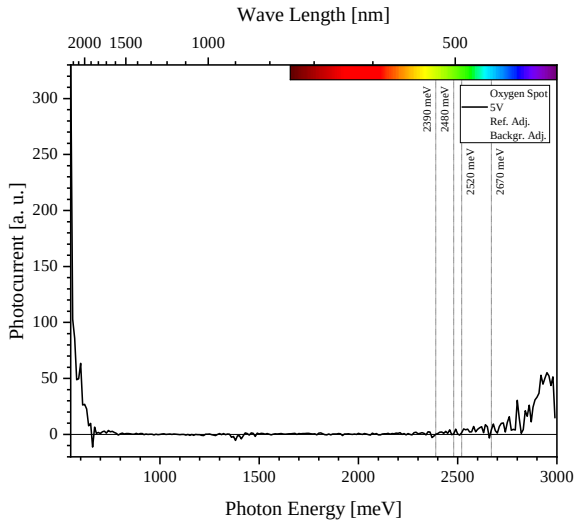

Figure 32: Normalized and background adjusted photocurrent data shown in linear scale of the diamond sample at the Oxygen implantation spot. Bias voltage is 5 V.

The other method for finding the starting point of the 5 V measurement, specifically the background adjustment, does not output a clear starting point either, as there are four crossings of the zero line in a region where all of them, when considering the noise, seem to be a suitable description of the starting point. These are 2390, 2480, 2520 and 2670 meV, as marked in figure 32. Looking at the raw data, the 2390 meV value seems to be the best approximation, not least because it matches the discretionary starting point fairly well.

In the no-photocurrent region of the raw data, see figure 31 (a) and (b), there are ostensibly no artifacts. The normalized data, shown in figure 31 (c) and (d), introduces the usual suspects of fake peaks where the laser power is particularly small. The only remaining option of finding a starting point therefore lies in evaluating the phase data.

Both raw data phase graphs, i.e. figure 33 (a) and (c), evince a strange apparent shift by about $+90°$. For reference, a line is drawn in these diagrams at that very value. It is not clear where this shift originates from. Shifting the 18°-threshold for the starting point in the moving-average-method correspondingly by $+90°$, the starting point is defined here as the energy at which the moving average leaves the $90° \pm 18°$ range. This results in the starting points at 2670 meV $(90° + 18°)$ for 0 V, 2370 meV $(90° - 18°)$ for 1 V, 2250 meV $(90° - 18°)$ for 2 V and 2250 meV $(90° - 18°)$ for 5 V.

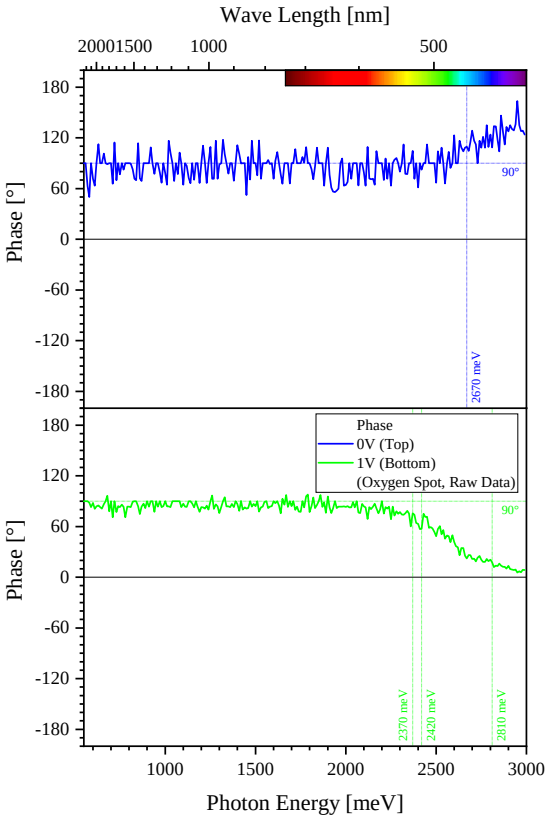

(a) Phase angle of Oxygen signal.

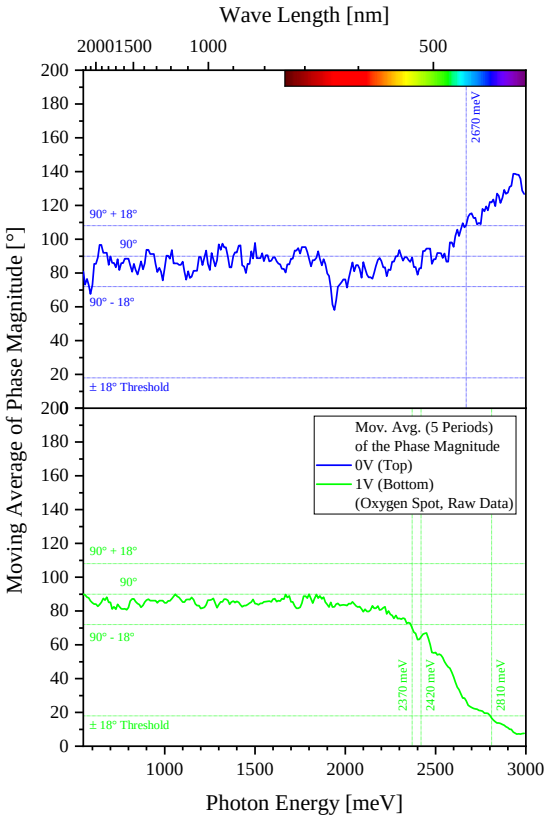

(b) Moving average of phase magnitude, 5 periods.

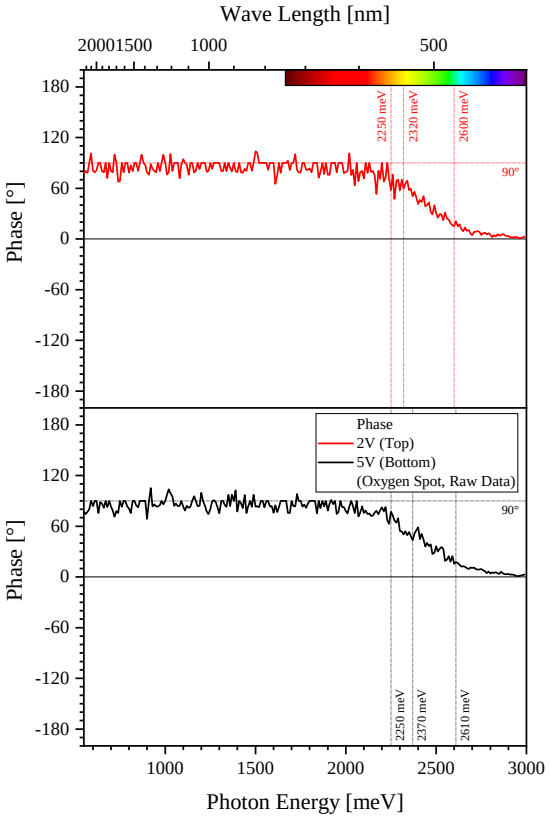

(c) Phase angle of Oxygen signal.

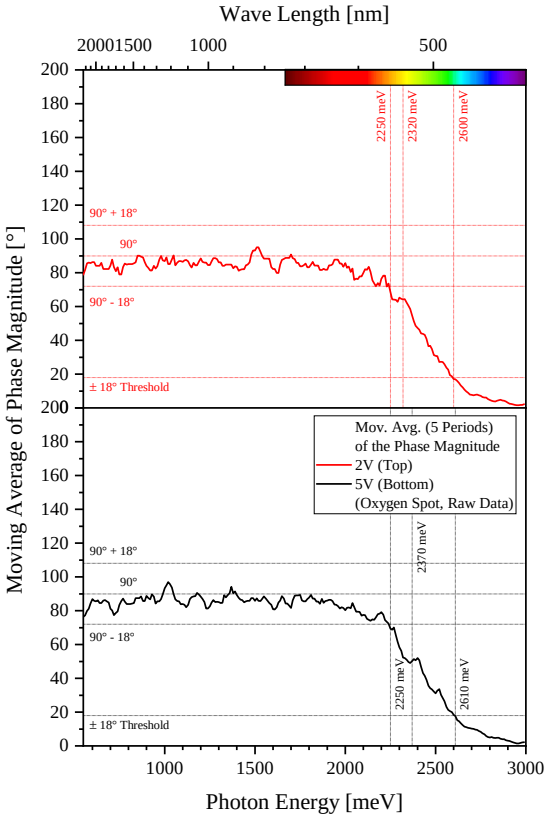

(d) Moving average of phase magnitude, 5 periods.

Figure 33: Phase data for the measurements from figure 31.

5.1.5 Sulphur

For the Sulphur spot, one data set was recorded with a bias voltage of 5 V. The resulting plots are shown in figures 34 and 35. In figure 34 (a) and (b), the maximum photocurrent at 2960 meV can be read off and it turns out to be 5.46 fA, coming in lower than the comparable Oxygen measurement but higher than the background. Similarly to the Oxygen measurement, there are no major artifacts outside of the noise range. As discussed previously, the normalized data in figure 34 (c) and (d) exhibits artificial peaks where the laser power distribution has its minima.

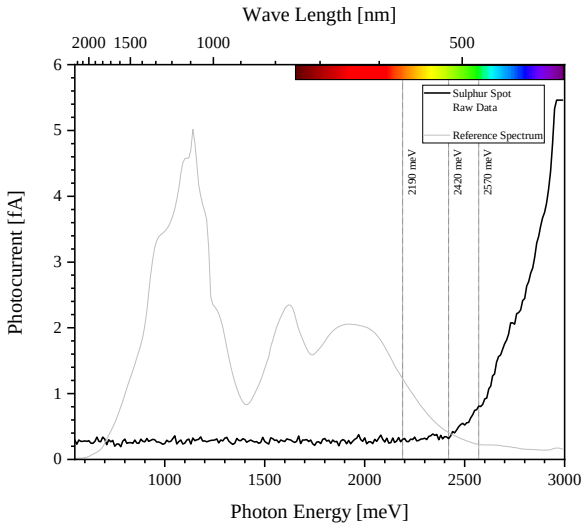

(a) Raw data, linear scale.

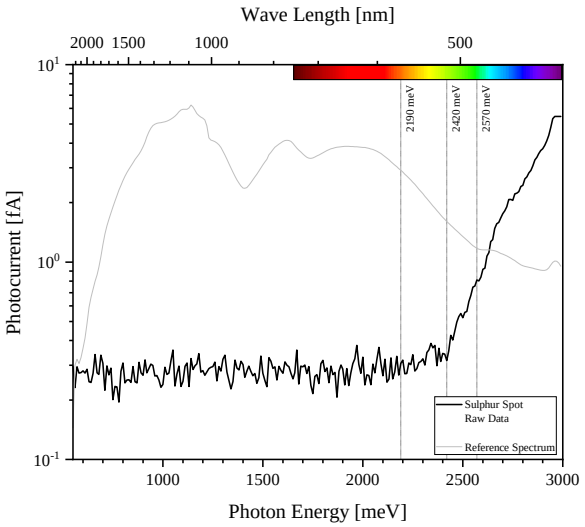

(b) Raw data, logarithmic scale.

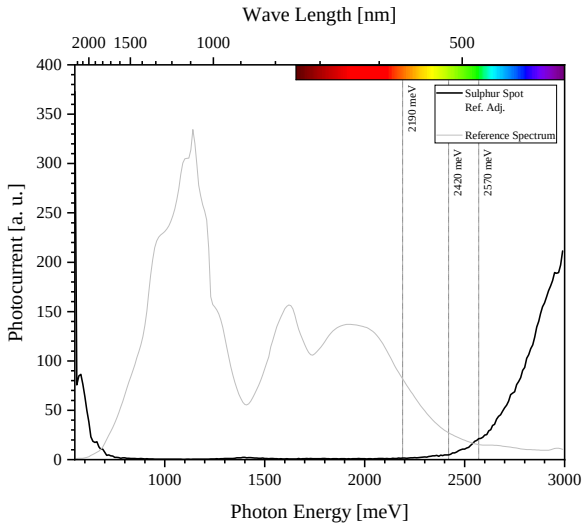

(c) Normalized data, linear scale.

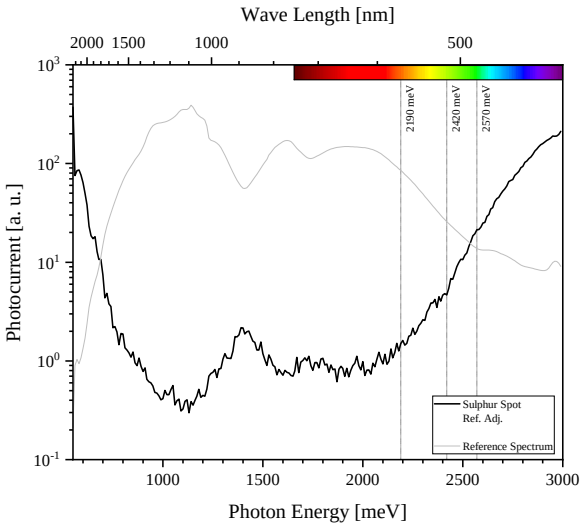

(d) Normalized data, logarithmic scale.

Figure 34: Photocurrent spectrum of the diamond sample at the Sulphur implantation spot. Bias voltage is 5 V. For phase data, see figure 35.

The phase data, see figure 35 (b), hovers around the 90° line and starts to deviate as the photocurrent increases. The moving-average-method finds the starting points at 2190 meV ($90° - 18°$) and 2570 meV (18°), as can be observed in figure 35 (c). Collating these values with the raw data, it seems that neither of the two are a very good match.

The last trough before the exponential increase seems to be at 2420 meV, although in the logarithmic chart, see figure 34 (b), the 2190 meV position could be interpreted as a very early starting point for an exponential curve. On the other hand, looking at the background adjusted data in figure 35 (a) does not yield further insight in this regard, as the last crossing of the zero line is at 2670 meV which is even further back than the 18° threshold intersection. In conclusion, the true starting point probably lies in the range of 2190 to 2420 meV.

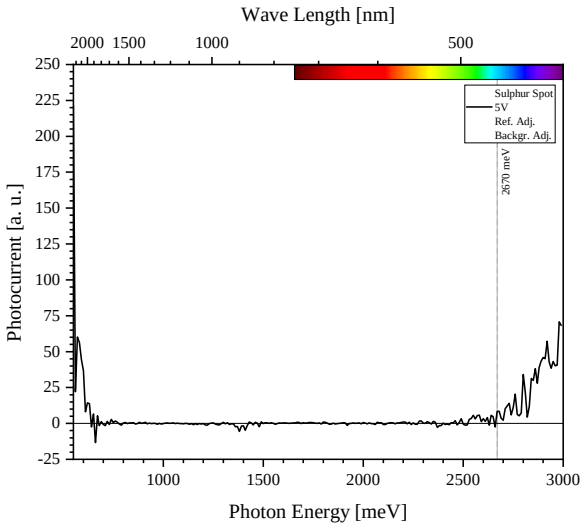

(a) Normalized and background adjusted, linear scale.

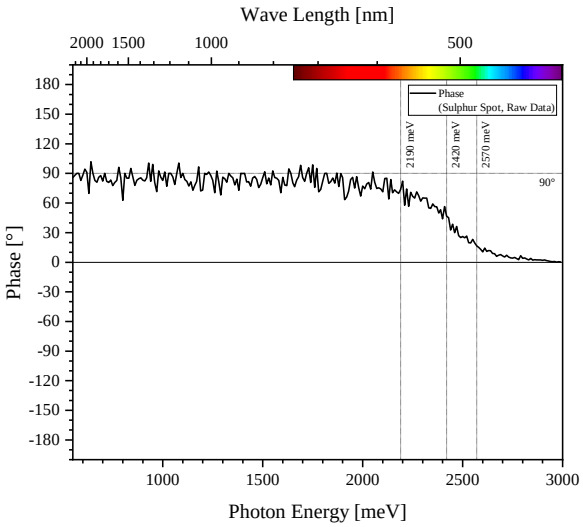

(b) Phase angle of Sulphur signal.

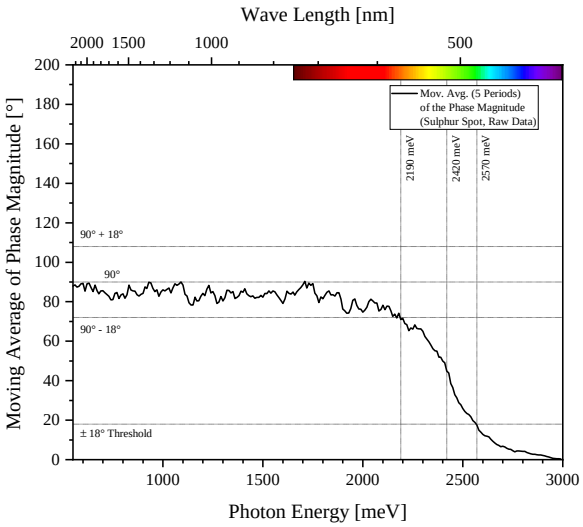

(c) Moving average of phase magnitude, 5 periods.

Figure 35: Background adjusted data and phase data for the measurements from figure 34.

5.1.6 Carbon-Nitrogen Molecule (CN)

For the CN spot, a total of four data sets were measured at bias voltages of 0, 1, 2 and 5 V, one for each, respectively. The corresponding diagrams are depicted in figures 36, 37 and 38. At the maximum of the photocurrent, see figure 36, which is located at 2970 meV for 0 V and at 2990 meV for 1, 2 and 5 V, the photocurrent peaks at 0.134, 2.06, 3.06 and 4.93 fA, respectively. Hence, the current is larger only by about 14.7% than the background, but smaller than all other implantation spots discussed thus far.

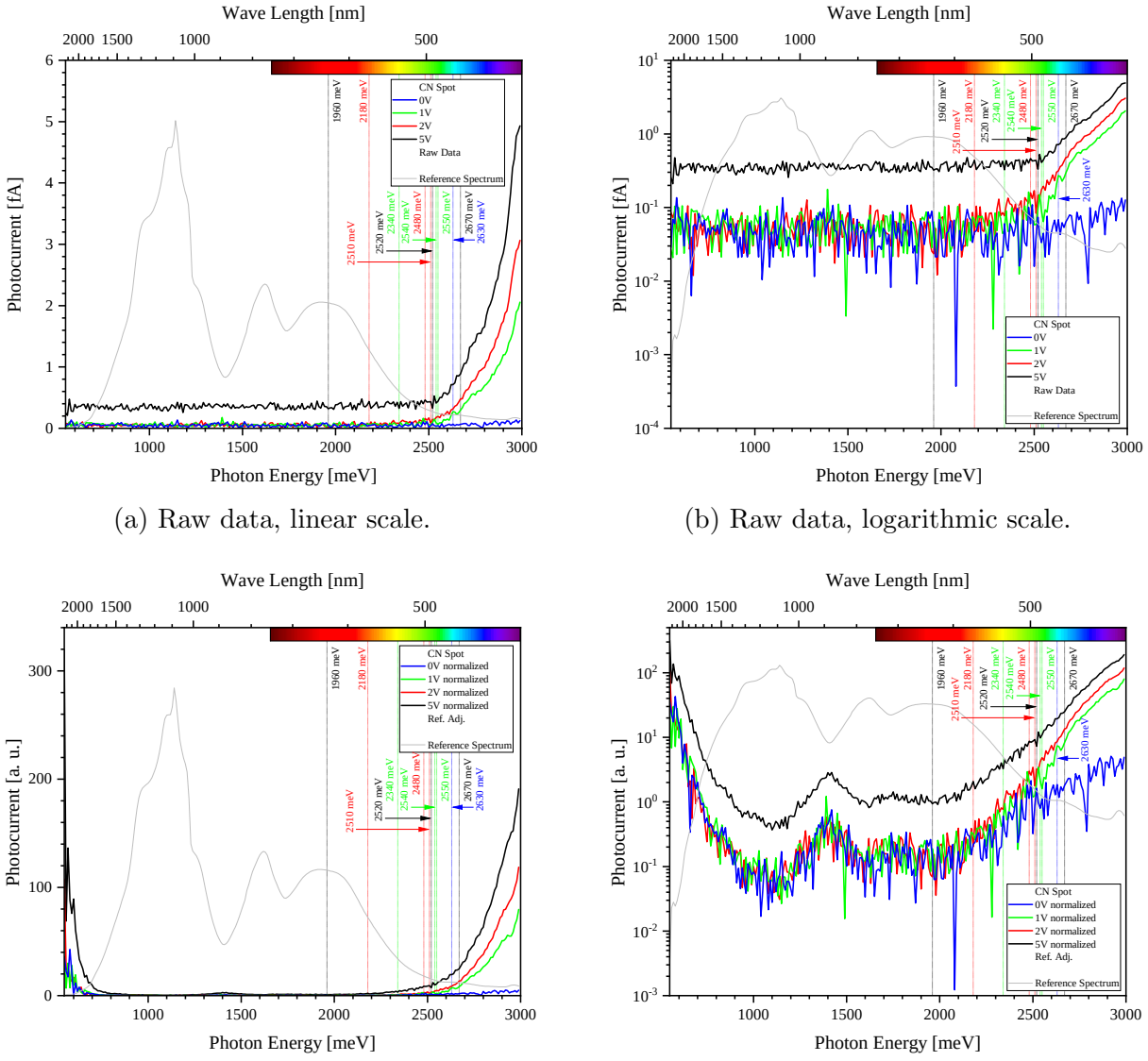

(a) Raw data, linear scale.

(b) Raw data, logarithmic scale.

(c) Normalized data, linear scale.

(d) Normalized data, logarithmic scale.

Figure 36: Photocurrent spectrum of the diamond sample at the CN implantation spot. Bias voltage is $0, 1, 2$ and 5 V. For phase data, see figure 38.

The phase data of all four measurements, shown in figure 38, once again oscillates around the 90°-line. Compared to the Oxygen data, for example, the fluctuation range is much broader in the CN data. The lock-in amplifier does not really seem to pick up a strong enough signal for the phase to converge to zero for the 0 V measurement, see figure 38 (a). Here, the moving average leaves the $90° \pm 18°$ range at 2630 meV, which approximately

matches what one might have estimated visually from the graph. Thus, this is considered the starting point of the photocurrent at a bias voltage of 0 V. In the other three data sets, the phase does tend to zero. Here, the $90° - 18°$ line is crossed at 2340, 2180 and 1960 meV in the 1, 2 and 5 V experiments. In the same sequence, the 18° threshold is reached at 2540, 2480 and 2670 meV. For all but the 1 and 2 V recording, the 18° starting point matches the raw data fairly well and likewise the $90° + 18°$ position for the 0 V measurement. However, the 5 V measurement starting point as determined in this way is completely off.

So, too, the background adjusted graph, as given in figure 37 is of no avail to this end as it shows a dip below the zero line in the interval from 2530 to 2880 meV, where it then finally goes back to positive terrain. The beginning of this interval almost coincides with what one would have guessed by choosing the last major trough in the raw 5 V data as the starting point, but given that the background adjusted data turns negative here, i. e. the photocurrent is less than that of the background, that match seems to be spurious. One possible explanation might be that the diamond itself has lots of Nitrogen impurities and so the additionally implanted CN does not contribute a lot to the overall signal. In order to obtain a starting point value for the 5 V data as well, the aforementioned trough at 2520 meV has to serve as the chosen value. For the 1 and 2 V data sets, the corresponding values are 2550 and 2510 meV. Unfortunately, the 0 V measurement simply does not have a strong enough signal that would allow choosing one of the many dips. Also, emphasis needs to be put on the absence of any raw data artifacts much like in the Sulphur and Oxygen spots of the preceding sections.

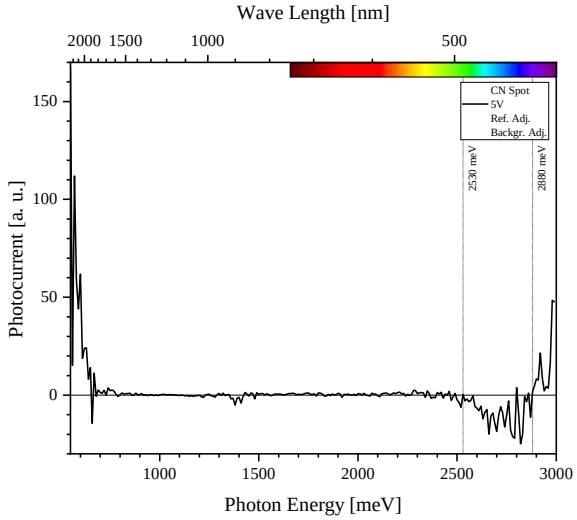

Figure 37: Normalized and background adjusted photocurrent data shown in linear scale of the diamond sample at the CN implantation spot. Bias voltage is 5 V.

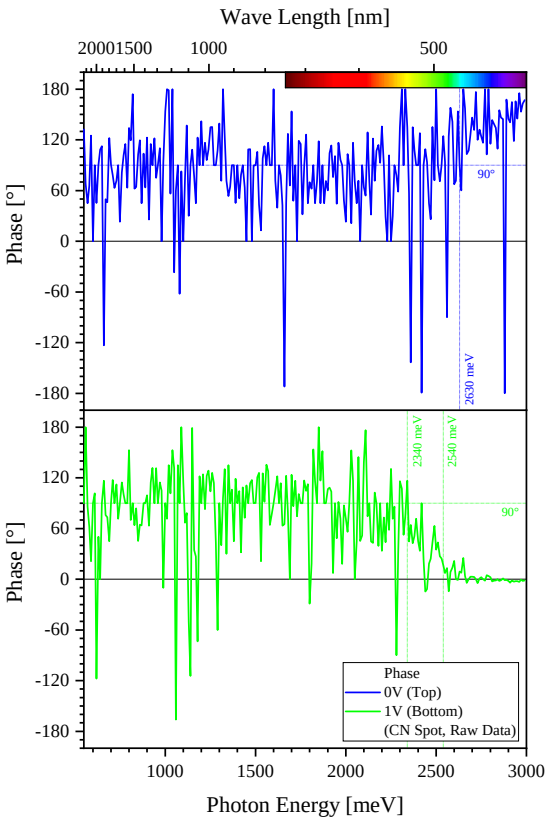

(a) Phase angle of CN signal.

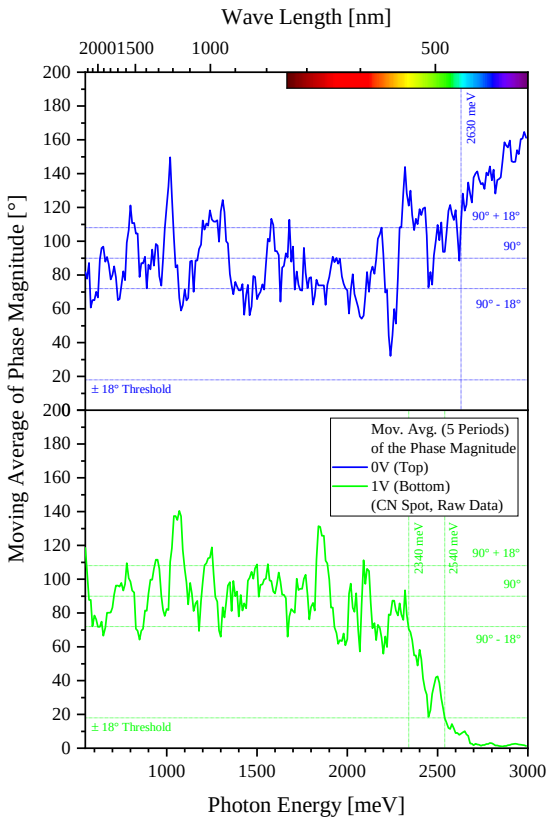

(b) Moving average of phase magnitude, 5 periods.

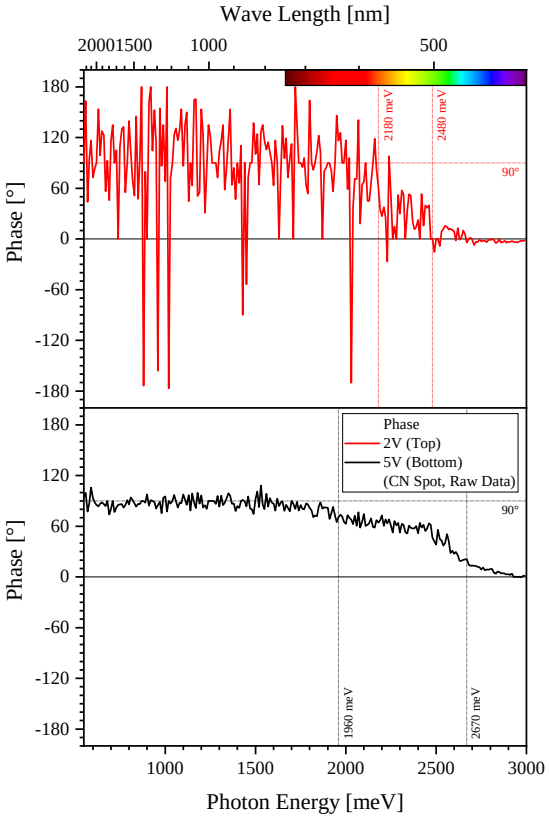

(c) Phase angle of CN signal.

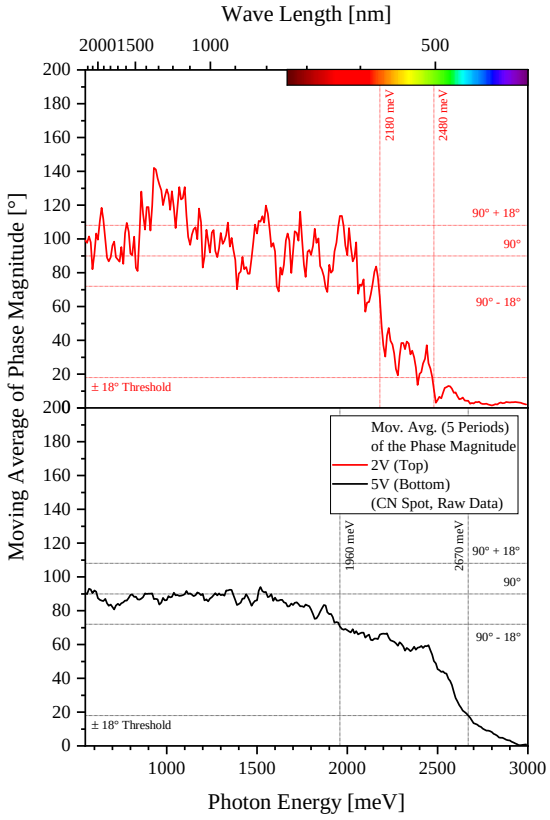

(d) Moving average of phase magnitude, 5 periods.

Figure 38: Phase data for the measurements from figure 36.

5.1.7 Annealed Carbon vs. Not-Annealed Carbon

For the Carbon implantation, two separate spots were irradiated of which one was treated before the diamond sample was put into the annealing oven (hereafter "annealed Carbon") and the other one was exposed to the ion beam only after the sample was annealed ("not-annealed Carbon" in the following). Both Carbon spots were measured at a bias voltage of 5 V and their data is plotted in figures 39, 40 and 41. At 2980 meV, both curves of the raw data reach their maximum. For the not-annealed spot it reaches 38.5 fA while the annealed Carbon comes in at 7.35 fA. This means that the photocurrent decreases by about -80.9% when the diamond is annealed.

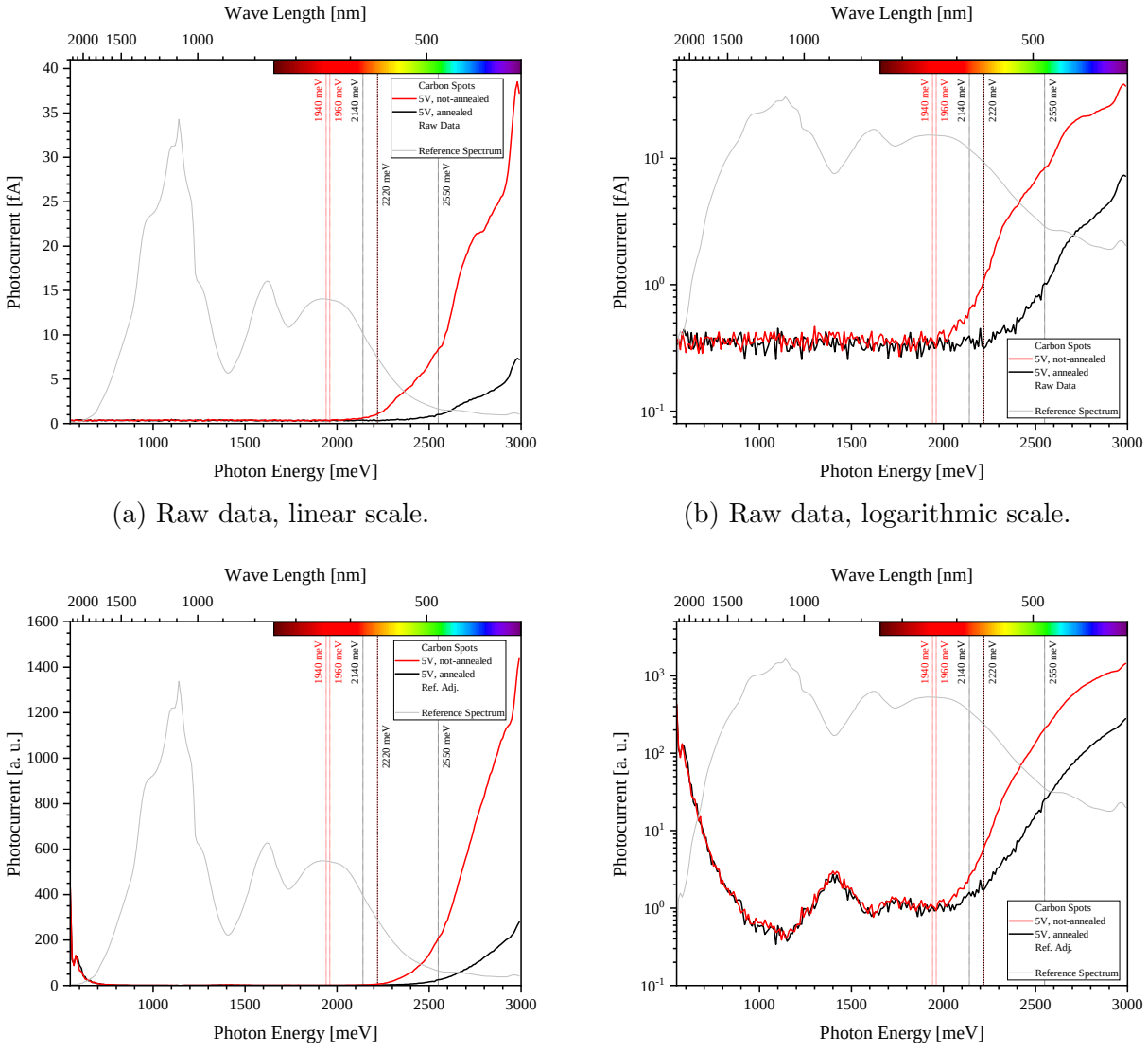

(a) Raw data, linear scale.

(b) Raw data, logarithmic scale.

(c) Normalized data, linear scale.

(d) Normalized data, logarithmic scale.

Figure 39: Photocurrent spectrum of the annealed and not-annealed diamond sample at the Carbon implantation spots. Bias voltage is 5 V. For phase data, see figure 41.

There are no noticeable artifacts in the raw data. As discussed earlier, the normalization introduces peaks where the reference spectrum has its minima, see figure 39 (c) and (d). Further, the photocurrent at the not-annealed Carbon spot seems to begin at a lower energy than the annealed. Perhaps this shift originates in the difference between the potentials of the less regular not-annealed diamond lattice and the more regular annealed diamond lattice. Or, the disparity arises from the laser power being too small at lower energies in order to detect a photocurrent there, meaning there is too much noise relative to the strength of the signal so that it does not get picked up by the measurement device. In principle, this can be an issue with all measurements subject to this Bachelor Thesis. In particular, the not-annealed Carbon photocurrent starts at 1960 meV while that of the annealed Carbon commences at 2220 meV, as determined by placing the starting points at the last troughs before the exponential increase.

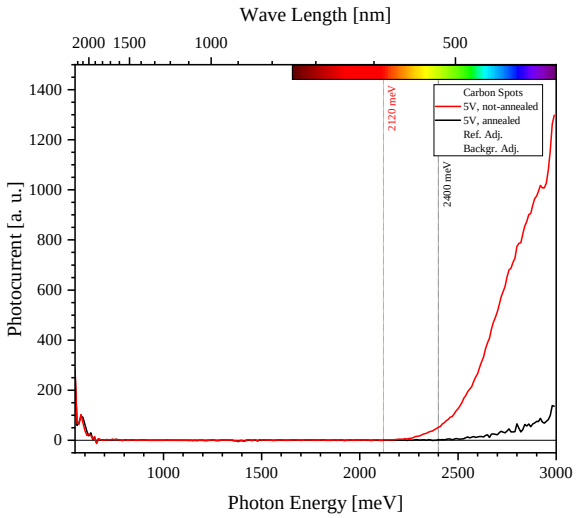

Figure 40: Normalized and background adjusted photocurrent data shown in linear scale of the diamond sample at the Carbon implantation spots, both for annealed and not-annealed Carbon. Bias voltage is 5 V.

The phase data, as shown in figure 41 (a), as well as the five-period moving average of the phase magnitude, depicted in figure 41 (b), oscillates around 90° before leaving the $90° \pm 18°$ range at 1940 meV in the not-annealed Carbon data set and at 2140 meV in the annealed Carbon data set. At 2220 meV, the moving average of the not-annealed Carbon spot reaches the 18° threshold while the corresponding energy for the annealed Carbon spot is 2550 meV. Notably, the fluctuation range of the phase data is quite narrow here.

Adjusting the normalized data for the background signal, as was done in figure 40, yields differing starting points for the two Carbon spots. The not-annealed Carbon data crosses the zero line at 2120 meV for the last time whereas at the annealed Carbon spot this point is at 2400 meV.

The only other feature of the Carbon data worth mentioning is the apparent reduction in the slope of the raw data photocurrent spectra in both Carbon data sets between ca. 2700 meV and 2900 meV. However, this is likely just due to the decrease of laser power at these energies because the corresponding region in the normalized diagrams does not show this to the same extent.

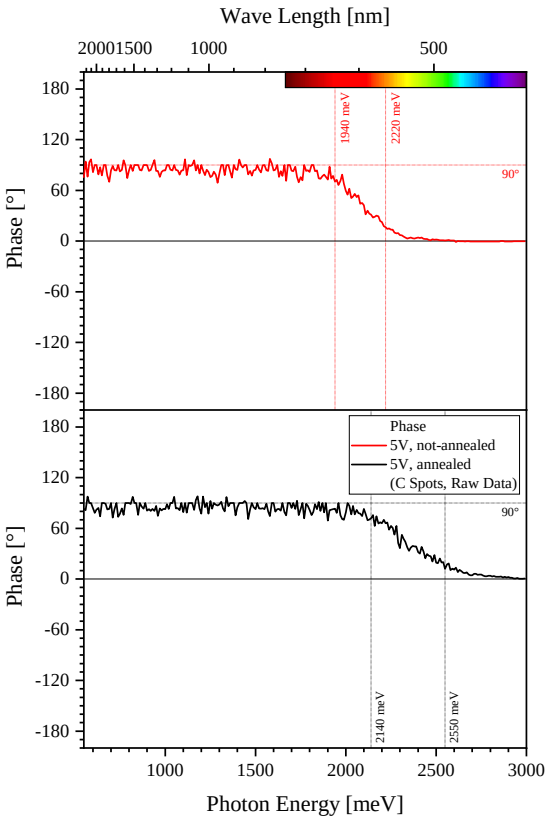

(a) Phase angle of Carbon signals.

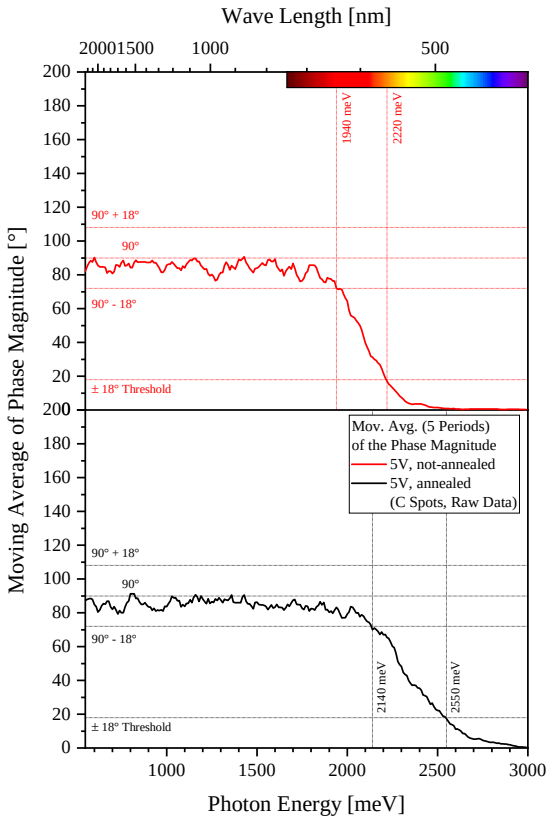

(b) Moving average of phase magnitude, 5 periods.

Figure 41: Phase data for the measurements from figure 39.

5.1.8 Photocurrent Dependence on Bias Voltage

Using the results of the previous sections allows for a comparison between the different implanted elements/molecules. In particular, figure 42 shows the maximum photocurrent that was obtained in the measurement range from 550 to 3000 meV with the white light laser. Even though the ordinate of this graph has units fA, this chart can only give an orientation of the relative size of the photocurrent between the elements because utilizing a different light source with a different intensity distribution will change the appearance of the individual measurements. However, what looks like a square-root-type dependence in figure 42 should exhibit a similar form when using another light source since this is a feature of the increasing bias voltage, while keeping everything else the same. Ordering by largest to smallest maximum photocurrent, the sequence is as follows: Carbon not-annealed > Boron > Phosphorus > Carbon annealed > Oxygen > Sulphur > CN > Background. It is affirmative to find the background measurement having the smallest of all peak photocurrents. On a final note, though, the magnitude of the photocurrent is also dependent on the amount of particles implanted. As this is not a constant over the various elements, it will certainly have an effect on these measurements as well. One could try to factor this into the ordinate of the data, but since the depth of the implantation is not entirely constant, it seems reasonable to conclude that this would introduce another dependence which cannot be accounted for within the scope of this Bachelor Thesis.

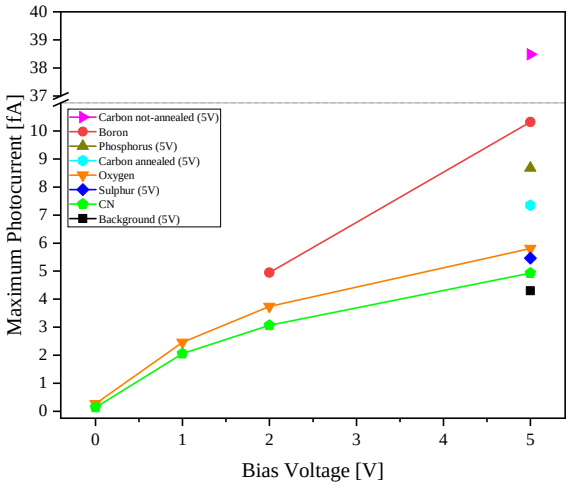

Figure 42: The dependence of the peak photocurrent on the bias voltage for all implanted particles.

5.1.9 Illumination vs. No Illumination Measurement

In figure 43, as expected, the stark difference between the sample with and without laser illumination is visible. This measurement was taken simply to show that there is indeed a difference between shining a laser on the diamond and turning it off again.

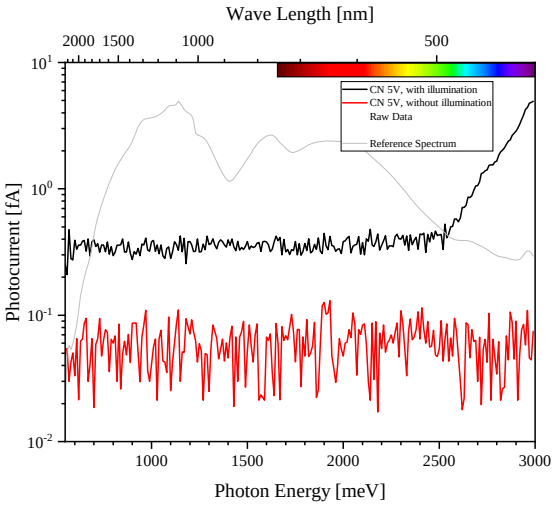

Figure 43: Measurement of the CN spot at a bias voltage of 5 V, with and without laser illumination.

5.1.10 Single-Switch vs. All-Switches

Since the laser illumination spot is not focused small enough to fit onto a single implantation only, there can be contaminations of the photocurrent signal if the incorrect switches are selected. For example, figure 44 shows the CN spot with only CN switched on and once with all implantations switched on. The latter exhibits the Boron dip around 1660 meV and from there on, all other elements are mixed into the signal giving rise to a larger photocurrent that the pure CN.

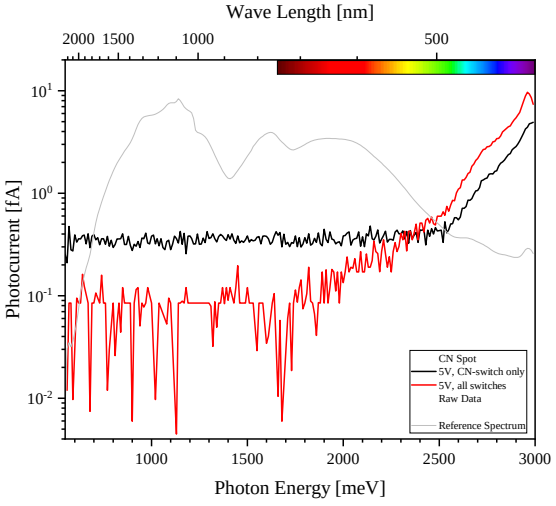

Figure 44: Photocurrent spectrum of the CN spot at a bias voltage of 5 V, with the CN switch only and with all switches selected.

5.1.11 Combined Elements

For an easier comparison, figure 45 shows the photocurrent spectrum in logarithmic scale with all implantation spots at a bias voltage of 5 V. Further, figure 46 displays the starting points as determined by the different methods. Here, they are stacked top to bottom from strongest maximum photocurrent to weakest, but the vertical position is not absolute. For the numerical values, see table 10.

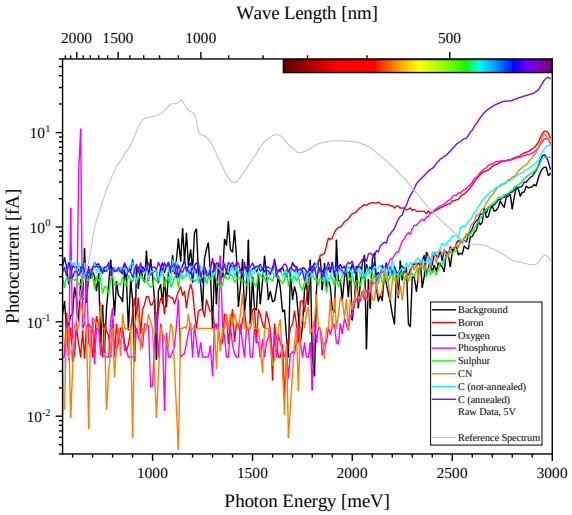

Figure 45: Photocurrent spectrum of all elements at a bias voltage of 5 V.

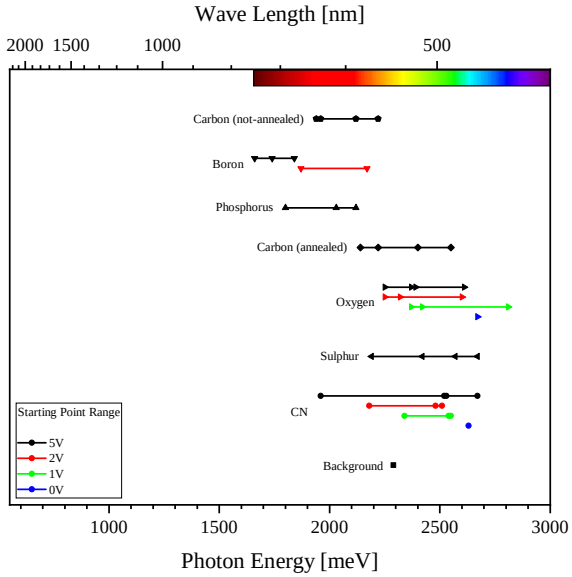

Figure 46: The starting points as discussed in the previous sections, see table 10 for the numerical value, or the corresponding section where the implantation spot was discussed.

Measurement		Starting Point Method				Maximum	
Element	Bias [V]	MA 90° ± 18° [meV]	MA 18° [meV]	NB Adj. [meV]	LT [meV]	E [meV]	PC [fA]
Carbon (n.a.)	5	1940	2220	2120	1960	2980	38.5
Boron	5	–	1740	1840	1660	2970	10.3
	2	–	2170	–	1870	2960	4.95
Phosphorus	5	–	2030	2120	1800	2970	8.68
Carbon (a.)	5	2140	2550	2400	2220	2980	7.35
Oxygen	5	2250	2610	2390	2370	2960	5.81
	2	2250	2600	–	2320	2960	3.74
	1	2370	2810	–	2420	2960	2.46
	0	2670	–	–	–	2950	0.267
Sulphur	5	2190	2570	2670	2420	2960	5.46
CN	5	1960	2670	2530	2520	2990	4.93
	2	2180	2480	–	2510	2990	3.06
	1	2340	2540	–	2550	2990	2.06
	0	2630	–	–	–	2970	0.134
Background	5	–	2290	–	2290	2960	4.30

Table 10: The photocurrent starting points as determined with the different methods. Also, the maximum photocurrent values are given and their corresponding energy position. Abbreviations:
"MA": Moving-average-method; "NB Adj.": Normalized and background adjusted data; "LT": Last trough, "E": Energy; "n.a.": not-annealed; "a.": annealed; "PC": Photocurrent.

5.2 Lithography Error Estimate

In order to gauge whether the measurements have any significant offset originating in the lithography mask, the sample is inspected under a microscope, particularly the implantation spots. All eight of them can be seen in figure 47, with lighting from below so that the deviations from the lithography mask can be viewed using an improved contrast. Moreover, in that figure the Palladium which is missing is marked in red, while the material that is too much is marked in green. The implantation spot is drawn in cyan. Assuming a simple linear relationship between Palladium coverage of the surface and the maximum photocurrent, these values can be scaled up as shown in table 11. Theoretically, within the circular structure, the lithography mask covers an area of about 26285 µm^2, and within the implantation region it covers approximately 16610 µm^2. Only Phosphorus and annealed Carbon switch places in both corrections, as shown in table 11. Sulphur switches with Oxygen only in the PC_{WA} correction.

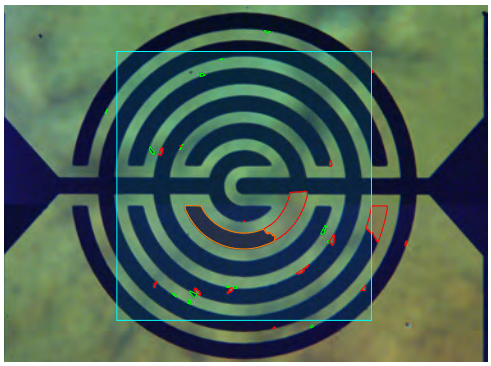

(a) Boron.

(b) Oxygen.

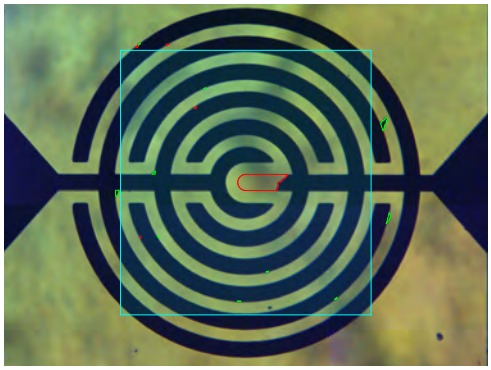

(c) CN.

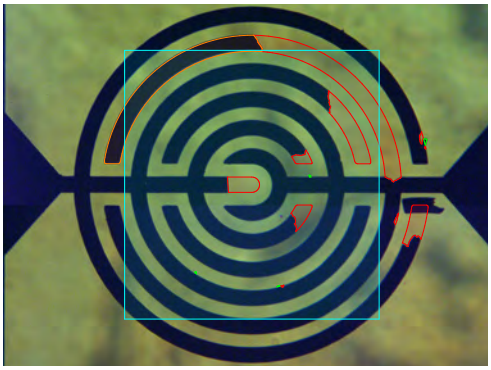

(d) Carbon (annealed).

(e) Phosphorus.

(f) Sulphur.

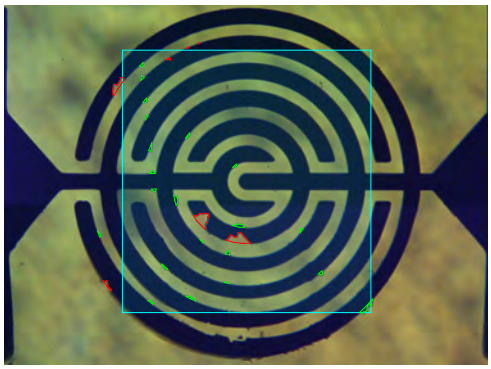

(g) Background.

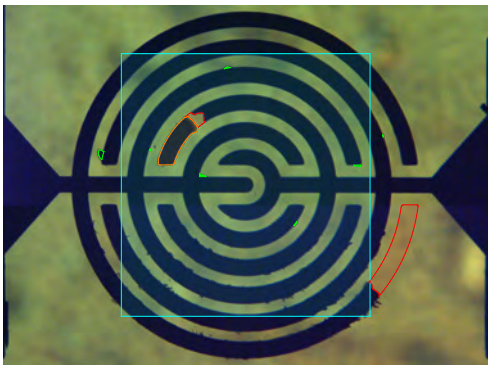

(h) Carbon (not-annealed).

Figure 47: Sample under a microscope at all eight implantation spots, at 20x magnification. The outermost circular ring has a diameter of 250 µm. For the schematic of the lithography mask, see figure 22.

El.	BV. [V]	Δ_{IA} [µm^2]	%	Act.A. [µm^2]	Δ_{WA} [µm^2]	%	Lith.A. [µm^2]	PC_M [fA]	PC_{IA} [fA]	PC_{WA} [fA]
$C_{(n.a.)}$	5	−510	−3.1	16100	−1290	−4.9	24995	38.5	39.7	40.5
B	5	−1128	−6.8	15482	−1334	−5.1	24951	10.3	11.1	10.9
	2							4.95	5.31	5.21
P	5	+30	+0.2	16640	+67	+0.3	26352	8.68	8.66	8.66
$C_{(a.)}$	5	−2595	−16	14015	−4267	−16	22017	7.35	8.71	8.77
O	5	N/A	N/A	N/A	N/A	N/A	N/A	5.81	N/A	N/A
	2							3.74		
	1							2.46		
	0							0.267		
S	5	−712	−4.3	15898	−3692	−14	22593	5.46	5.71	6.35
CN	5	−338	−2.0	16272	−344	−1.3	25941	4.93	5.03	5.00
	2							3.06	3.13	3.10
	1							2.06	2.10	2.08
	0							0.134	0.137	0.136
Back.	5	−44	−0.3	16566	−83	−0.3	26201	4.30	4.31	4.31

Table 11: Correction of the Maximum Photocurrent by estimating the error from the lithography. Abbreviations:
"El.": **El**ement; "(a.)": **a**nnealed; "(n.a.)": **n**ot-**a**nnealed; "Back.": **Back**ground; "BV.": **B**ias **V**oltage; "Δ_{IA}": Deviation from the theoretical mask in the **i**mplantation **a**rea; "Act.A.": **Act**ive **A**rea, i. e. the surface coverage that is able to measure within the implantation region; "Δ_{WA}": Deviation from the theoretical mask in the **w**hole **a**rea of the circular structure; "Lith.A.": **Lith**ographed **A**rea, i. e. Act.A. plus the coverage of lithographed material outside the implantation area but within the circular structure; "PC_M": Measured Maximum Photocurrent, see previous sections; "PC_{IA}": $= \frac{PC_M}{1+\Delta_{IR}(\%)}$, i. e. Photocurrent scaled using the percentage from Δ_{IA}; "PC_{WA}": $= \frac{PC_M}{1+\Delta_{WA}(\%)}$, i. e. Photocurrent scaled using the percentage from Δ_{WA}. Note: The lithography at the Oxygen spot shows no significant imperfections.

6 Conclusion

The amplitude of the maximum photocurrent at 5 V can be ordered as follows [fA]: Carbon (not-annealed) 38.5 > Boron 10.3 > Phosphorus 8.68 > Carbon (annealed) > 7.35 > Oxygen 5.81 > Sulphur 5.46 > CN 4.93 > Background 4.30. Further information can be found in table 10 and table 11, where estimates for the errors of these values emanating from the experimental implementation of the lithography are given, too.

The former table also summarizes the starting energies of the photocurrent. Looking at the 5 V raw data and determining them discretionarily, the order turns out to be [meV]: Boron 1660 < Phosphorus 1800 < Carbon (not-annealed) 1960 < Carbon (annealed) 2220 < Background 2290 < Oxygen 2370 < Sulphur 2420 < CN 2520.

From the collected data it was further possible to deduce the dependence of the maximum photocurrent on the bias voltage which is seems to be of the form of a square root graph, as illustrated in figure 42. As a proof of concept that the recorded data is indeed a real signal and not just randomly collected noise, a measurement with and without the laser was taken and the difference between the two becomes clear when looking at figure 43. Moreover, there is a noticeable impact on the data if the incorrect switch is selected for the measurement of only one implantation spot. In figure 44, this distinction is visible where the same measurements were taken once with the correct switch and once with all switches. Notably, both the starting energy and the maximum photocurrent differs greatly when comparing annealed and not-annealed Carbon, in particular the maximum photocurrent reaches about 5.2 times higher with not-annealed Carbon.

For further studies, it may be advantageous to use a light source that has a more stable spectrum and a higher intensity. Moreover, it may be interesting to expand the energy range for there could be deviations from the noise in the low energy end or additional peaks, at both ends of the measurement range. In addition, the dependence of the photocurrent on the bias voltage may be investigated in further detail by collecting data points at larger number of voltages.

This Bachelor Thesis was conducted as part of the Applied Quantum Systems group at Leipzig University to contribute to the understanding of the properties of defects in diamond by means of characterizing the photocurrent spectra, for which there exists currently only very little experimental data. The findings of this bachelor thesis may facilitate the comprehension of use cases of different defects in quantum applications in the future.

References

[1] Kungliga Vetenskapsakademien. *Nobelpriset Fysik 1921*. URL: https://www.kva.se/prisvinnare/albert-einstein/.

[2] National Center for Biotechnology Information. *National Library of Medicine*. URL: https://pubchem.ncbi.nlm.nih.gov/element/6.

[3] Asbury Carbons. *Structural Description [of Graphite]*. URL: https://asbury.com/de/informationsangebot/education/graphite-101/structural-description/.

[4] Own creation, inspired by Chemistry LibreTexts. *Hybridization*. URL: https://chem.libretexts.org/Ancillary_Materials/Reference/Organic_Chemistry_Glossary/Hybridization.

[5] Scientific American. *How can graphite and diamond be so different if they are both composed of pure carbon?* URL: https://www.scientificamerican.com/article/how-can-graphite-and-diam/.

[6] Steve Sque. *Structure of Diamond*. URL: https://www.stevesque.com/diamond/structure/.

[7] Own creation, inspired by Steve Sque. *Structure of Diamond*. URL: https://www.stevesque.com/diamond/structure/.

[8] Element Six / De Beers Group. *The Element Six CVD Diamond Handbook*. URL: https://e6cvd.com/media/wysiwyg/pdf/E6_CVD_Diamond_Handbook_A5_v10X.pdf.

[9] FH Münster. *Physical Properties of Selected Optical Materials at Room Temperature*. URL: https://www.fh-muenster.de/ciw/downloads/personal/juestel/juestel/Bandgaps-Densities-IEPs-RefractiveIndices.pdf.

[10] Nikolai Teofilov. *Optical Investigations on the Wide Bandgap Semiconductors Diamond and Aluminumnitride*. Dissertation, 2007. URL: https://www.osti.gov/etdeweb/servlets/purl/21252592.

[11] Kelly Gordon. *Color Quality of White LEDs*. URL: https://cool.culturalheritage.org/byorg/us-doe/color_quality_of_white_leds.pdf.

[12] Own creation, inspired by H. M. King / Geology.com. *Yellow Diamonds*. URL: https://geology.com/diamond/yellow-diamonds/.

[13] Own creation, inspired by Dipartimento di Chimica / Università di Torino. *Defects in Diamond with the CRYSTAL Code*. URL: https://www.crystal.unito.it/vibs/defects/diamond.html.

[14] Y. Zheng, C. Li, J. Liu, J. Wei, and H. Ye. "Diamond with Nitrogen: States, Control and Applications". In: *Functional Diamond* 1 (Jan. 2021), pp. 1–30. DOI: 10.1080/26941112.2021.1877021.

[15] Gemological Institute of America. *Visible Absorption Spectra of Colored Diamonds*. URL: https://www.gia.edu/doc/GG-Spring-2015-foldout.pdf.

[16] S. Eaton-Magaña C. M. Breeding and J. E. Shigle. "Naturally Colored Yellow and Orange Gem Diamonds: The Nitrogen Factor". In: *Gems & Gemology* 56 (Summer 2020), pp. 194–219. DOI: http://dx.doi.org/10.5741/GEMS.56.2.194.

[17] Gemological Institute of America. *Optical Defects in Diamond: A Quick Reference Chart*. URL: https://www.gia.edu/gems-gemology/summer-2013-shigley-optical-defects-diamond.

[18] (Fig. 4 (c) and (e) inspired by) C. M. Breeding, S. Eaton-Magaña, and J. E. Shigley. "Natural-Color Green Diamonds: A Beautiful Conundrum". In: *Gems & Gemology* 54 (Spring 2018), pp. 2–27. DOI: http://dx.doi.org/10.5741/GEMS.54.1.2.

[19] L. Pham, N. Bar-Gill, D. Sage, A. Stacey, M. Markham, D. Twitchen, M. Lukin, and R. Walsworth. "Enhanced Metrology Using Preferential Orientation of Nitrogen-Vacancy Centers in Diamond". In: *Physical Review B* 86 (July 2012). DOI: 10.1103/PhysRevB.86.121202.

[20] Own creation, inspired by H. M. King / Geology.com. *Blue Diamonds*. URL: https://geology.com/diamond/blue-diamonds/.

[21] Adapted from Leipzig University, AQS. *100 kV Implanter*. URL: https://www.physgeo.uni-leipzig.de/en/fbi/aqs/research/equipment#collapse434315.

[22] Own creation, inspired by Lasse Rad. *Farbzentren in Siliziumkarbid mittels Implantation von H, O, F, Cl, Ge, Sn, I und Br*. Bachelor Thesis, 2021. URL: https://www.physgeo.uni-leipzig.de/fileadmin/Fakult%C3%A4t_PhysGeo/FBI/Dokumente/AQS/Forschung/RadL-Bachelorarbeit-2021.pdf.

[23] National Electrostatics Corp. *Source of Negative Ions by Cesium Sputtering (SNICS)*. URL: https://www.pelletron.com/wp-content/uploads/2017/02/SNICS-v2.pdf.

[24] Own creation, inspired by Manuel Kuhrke. *Erzeugung von Einkristall Diamantmembranen mit NV-Zentren*. Bachelor Thesis, 2021. URL: https://www.physgeo.uni-leipzig.de/fileadmin/Fakult%C3%A4t_PhysGeo/FBI/Dokumente/AQS/Forschung/KuhrkeM-Bachelorarbeit-2021.pdf.

[25] National Electrostatics Corp. *General Purpose Acceleration Tube*. URL: https://www.pelletron.com/products/acceleration-tubes/#GP.

[26] The NIST Reference on Constants, Units, and Uncertainty. *Fundamental Physical Constants*. URL: https://physics.nist.gov/cgi-bin/cuu/Value?e.

[27] NIST Chemistry WebBook, SRD 69. *Hydrogen Anion*. URL: https://webbook.nist.gov/cgi/cbook.cgi?ID=C12184882&Mask=20.

[28] The NIST Reference on Constants, Units, and Uncertainty. *Fundamental Physical Constants*. URL: https://physics.nist.gov/cgi-bin/cuu/Value?c.

[29] Leipzig University, AQS. *High Temperature Furnace*. URL: https://www.physgeo.uni-leipzig.de/en/fbi/aqs/research/equipment#collapse469959.

[30] The LayoutEditor. URL: https://layouteditor.com/.

[31] Microchemicals. *AZ® nLOF 2000 Serie*. URL: https://www.microchemicals.com/products/photoresists/az_nlof_2020.html.

[32] ShinEtsu Microsi. *The Difference Between Positive and Negative Photoresist*. URL: https://www.microsi.com/blog/the-difference-between-positive-and-negative-photoresist/.

[33] Own creation.

[34] Microchemicals. *TechniStrip® NI555*. URL: https://www.microchemicals.com/products/remover_stripper/technistrip_ni555.html.

[35] Ptable. *Periodic Table.* URL: https://ptable.com/?lang=en.

[36] Tobias Lühmann. *Ionenstrahl-Modifikation von Diamant zur optimierten Farbzentrenbildung als Wegbereiter für skalierbare Quantentechnologien*. Dissertation, 2021. URL: https://nbn-resolving.org/urn:nbn:de:bsz:15-qucosa2-761435.

[37] James F. Ziegler. *The Stopping and Range of Ions in Matter Software*. URL: http://www.srim.org/.

[38] Own creation, inspired by F. Schein and A. Lajn (Semiconductor Physics Group at Leipzig University). URL: https://research.uni-leipzig.de/hlp/.

The resources linked to in these references were present as of February 5, 2023. The URLs/DOIs may be subject to change in the future.

Acknowledgements

Finally, I would like to express my gratitude to everyone who helped me in the course of my work for this Bachelor Thesis, especially my supervisors Prof. Dr. Jan Berend Meijer and Dr. Sébastien Pezzagna.

Further, I want to explicitly mention and thank Dr. Tobias Lühmann for helping me with the ion implantation using the 100kV-accelerator and subsequent annealing, as well as Dominic Reinhardt for his support in the various lithography-related processes, and Tanja Jawinski and Dr. Lukas Trefflich for their assistance during the measurements of the diamond sample, and Sascha Becker for his advice on experimental parameters and the design of the implantation mask.

Last but not least, I would like to thank my family for their support throughout my bachelor studies.

Declaration of Authorship

I hereby certify that this Bachelor Thesis has been composed by myself and describes my own work. Where I have consulted the work of others this is always clearly stated. All statements taken literally from other writings or referred to by analogy are marked and the source is always supplied. This thesis has not been accepted in any previous application for a degree.

Leipzig, February 9, 2023

Tobias Erbacher